Frontiers in Bioscience Landmark

Front. Biosci. (Landmark Ed) **2026**; 31(10): 55577
https://doi.org/10.31083/FBL55577

Original Research

Sodium Butyrate Ameliorates Hepatic Steatosis and Insulin Resistance in MASLD Models With Concurrent Alterations in AMPK and PI3K/AKT Signaling

Yinan Zhao[1], Ping Jiang[2], Yiwen Zhang[1], Ya Wang[1], Yige Wang[1], Guoying Yu[3,*]

[1]Clinical Medical College of Qinghai University, 810000 Xining, Qinghai, China
[2]Qinghai University Medical College, 810016 Xining, Qinghai, China
[3]Department of Hepatology II, Fourth People's Hospital of Qinghai Province, 810000 Xining, Qinghai, China
*Correspondence: ygyqh999@126.com (Guoying Yu)

Academic Editor: Vesna Jacevic
Submitted: 3 July 2026 Revised: 26 August 2026 Accepted: 3 September 2026 Published: 14 October 2026

Abstract

Background: Metabolic dysfunction-associated steatotic liver disease (MASLD) is characterized by dysregulated glucose and lipid metabolism and is closely linked to insulin resistance (IR). Sodium butyrate (NaB) is a short-chain fatty acid with reported metabolic benefits, but its effects on MASLD-related IR remain unclear. This study investigated the therapeutic efficacy of NaB in both palmitate (PA)-induced insulin-resistant hepatocytes and high-fat diet (HFD)-induced MASLD in mice and to elucidate the underlying mechanisms responsible for its effects. **Methods:** We evaluated the effects of NaB in PA-treated HepG2 cells and in C57BL/6 mice fed an HFD for 16 weeks followed by 8 weeks of oral NaB administration. Lipid accumulation, glucose metabolism, glycogen storage, transcriptomic changes, and adenosine monophosphate-activated protein kinase (AMPK) and phosphoinositide 3-kinase/protein kinase B (PI3K/AKT) signaling were assessed using biochemical assays, staining, reverse transcription-quantitative polymerase chain reaction (RT-qPCR), western blotting, RNA sequencing, and detection of inflammatory activity. **Results:** In PA-treated HepG2 cells, NaB reduced lipid accumulation, improved glucose uptake and glycogen storage, and reduced the secretion of the pro-inflammatory mediators tumor necrosis factor-α (TNF-α), interleukin-6 (IL-6), interleukin-1β (IL-1β), and monocyte chemoattractant protein-1 (MCP-1) in a dose-dependent manner. These effects were accompanied by the restoration of G protein-coupled receptor 43 (GPR43)/calcium/calmodulin-dependent protein kinase kinase 2 (CaMKK2)/AMPKα/sirtuin 1 (SIRT1) signaling and the activation of PI3K/AKT signaling, with decreased lipogenesis, enhanced fatty acid oxidation, reduced gluconeogenic gene expression, and alleviation of the cellular inflammatory response. In HFD-fed mice, NaB reduced body weight gain, improved serum and hepatic lipid profiles, attenuated hepatic steatosis, improved glucose tolerance and insulin sensitivity, and increased hepatic glycogen storage, while markedly lowering circulating and intrahepatic pro-inflammatory cytokine levels and downregulating hepatic expression of the macrophage marker F4/80 to mitigate inflammatory infiltration of the liver. **Conclusion:** These results demonstrate that NaB administration alleviated hepatic steatosis and IR in MASLD models, with these effects coinciding with the coordinated regulation of AMPK and PI3K/AKT signaling. While NaB may serve as a metabolic modulator, further mechanistic validation of dual-pathway crosstalk, characterization of inflammatory responses, and translational research are still needed.

Keywords: butyric acid; insulin resistance; nonalcoholic fatty liver disease; AMP-activated protein kinases; phosphatidylinositol 3-kinase/akt signaling pathway

1. Introduction

Metabolic dysfunction-associated steatotic liver disease (MASLD; previously referred to as non-alcoholic fatty liver disease or NAFLD) has become the most common chronic liver disease worldwide, affecting an estimated 25% to 30% of the general population and over 50% of individuals diagnosed with type 2 diabetes mellitus or obesity [1]. A key pathological hallmark of MASLD is insulin resistance (IR), particularly at the hepatic level [2]. Hepatic IR interferes with the homeostatic balance between lipid uptake, de novo lipogenesis, fatty acid β-oxidation, and lipid export, leading to excessive triglyceride accumulation within hepatocytes [2,3]. In individuals affected by hepatic IR, insulin fails to properly suppress gluconeogenic output, and fasting glucose therefore tends to rise [4]. This hepatic IR state may also intensify metabolic dysfunction in peripheral tissues, thereby exacerbating hepatic fat accumulation and systemic metabolic disorders [4,5]. Despite a growing understanding of the epidemiology and clinical presentation of MASLD, treatment options remain limited [6,7].

Disrupted intracellular signaling is an important contributor to the metabolic phenotype that defines MASLD [8,9]. Among these signaling pathways, the phosphoinositide 3-kinase/protein kinase B (PI3K/AKT) axis plays an important role in relaying insulin signaling within hepatocytes [10]. In these cells, insulin binding to its cognate receptors triggers the receptor-dependent phosphorylation

Copyright: © 2026 The Author(s). Published by IMR Press.
This is an open access article under the CC BY 4.0 license.

Publisher's Note: IMR Press stays neutral with regard to jurisdictional claims in published maps and institutional affiliations.

of insulin receptor substrate 1/2 (IRS1/2), which then activates PI3K and promotes downstream AKT-mediated signaling [8]. Once activated, AKT inhibits gluconeogenic regulators such as forkhead box O1 (FOXO1) and regulates glycogen synthase kinase 3β (GSK3β). Insulin-dependent glucose uptake in peripheral muscle and adipose tissues relies on GLUT4 translocation, whereas hepatocytes express GLUT2 to mediate bidirectional glucose flux under the control of hepatic insulin signaling, supporting intrahepatic glycogen synthesis and gluconeogenesis. Of note, direct literature evidence documenting insulin-AKT-dependent regulation of hepatic GLUT2 is unavailable, and this regulatory relationship is partially supported by our present experimental observations. In parallel with these processes, adenosine monophosphate-activated protein kinase (AMPK) functions as a key sensor of cellular energy status, contributing to both the suppression of lipogenesis and the enhancement of mitochondrial fatty acid oxidation [9]. In MASLD, reduced AMPK activity is often associated with increased lipid production, impaired β-oxidation, and decreased responsiveness to insulin [9,11]. Importantly, the activity of the PI3K/AKT and AMPK pathways is not independent, as the two are functionally intertwined. AMPK activation may relieve lipotoxic stress and enhance insulin sensitivity, whereas the preservation of PI3K/AKT signaling is necessary for effective hepatic glucose uptake, utilization, and storage [8,12,13]. However, there remains a lack of therapeutic strategies capable of simultaneously targeting both of these signaling pathways.

Of the many metabolites produced by the gut microbiota, sodium butyrate (NaB) has attracted increasing attention owing to its broad metabolic effects [14,15]. As a major short-chain fatty acid (SCFA), NaB can act through G protein-coupled receptors 43 and 41 (GPR43/GPR41) and can also regulate transcriptional activity by inhibiting histone deacetylases (HDACs) [16,17]. Previous studies have suggested that NaB may activate the GPR43/AMPK axis, suppress lipogenesis, and enhance fatty acid oxidation [16,18]. Other studies indicate that NaB may also improve insulin-related signaling, including IRS1 and AKT phosphorylation, thereby benefiting glucose metabolism [19,20]. However, current research on this topic remains limited. In particular, relatively little is known as to whether, in the context of MASLD-related IR, NaB can simultaneously alleviate lipid and glucose metabolic dysfunction while also modulating AMPK and PI3K/AKT signaling activity. Prior studies have separately characterized NaB-mediated AMPK activation or the improvement of insulin-related PI3K/AKT signaling, but descriptions of any coordinated dual-pathway regulatory activity associated with MASLD-related IR remain lacking, and there have not been any instances of the functional validation of this coordinated regulatory effect.

In the present study, we established palmitate (PA)-treated HepG2 cells and high-fat diet (HFD)-fed mice to evaluate whether NaB can alleviate glycolipid metabolic disturbances associated with MASLD-related IR. We further examined whether changes in lipid accumulation, glucose uptake, glycogen storage, and metabolic gene and protein expression coincide with alterations in AMPK and PI3K/AKT signaling. By integrating phenotypic, biochemical, transcriptomic, and molecular analyses, the overall aim of this study was to characterize the metabolic response pattern associated with NaB treatment and to provide a more coherent experimental basis for understanding its role in MASLD.

2. Materials and Methods

2.1 Reagents, Antibodies, and Cell Culture

NaB (R21524) was obtained from Shanghai Yuanye Biotechnology Co., Ltd. PA and its solvent (vehicle) were purchased from Kunchuang Technology (Xi'an, Shaanxi, China). All working solutions were freshly prepared before each experiment. Human HepG2 hepatoma cells (Wuhan Pricella Biotechnology Co., Ltd.) were cultivated in Dulbecco's Modified Eagle Medium (DMEM; Gibco, USA) containing 10% fetal bovine serum (Gibco) and 1% penicillin–streptomycin (Pricella). Cells were cultured at 37 °C in a humidified incubator under 5% CO_2. For routine experiments, cells were seeded and allowed to adhere overnight before drug treatment.

All commercial biochemical assay kits were purchased from Nanjing Jiancheng Bioengineering Institute Co., Ltd., including a glucose detection kit (A154-1-1), triglyceride (TG) kit (A110-1-1), total cholesterol (TC) kit (A111-1-1), non-esterified fatty acid (NEFA) kit (A042-2-1), and bicinchoninic acid (BCA) total protein quantification kit (A045-4). A Human Glycogen ELISA kit (YOBIBIO, U96-1904E) was used to quantify glycogen levels. Oil Red O and the periodic acid–Schiff (PAS) glycogen staining kits were sourced from Solarbio (G1262 and G1360, respectively), while the mounting media consisted of glycerol-gelatin (Servicebio). Unless indicated otherwise, all other reagents were of analytical grade. Primary antibodies used for immunoblotting were specific for GPR43, CaMKK2 and phospho-CaMKK2, AMPKα, phospho-AMPKα, SIRT1, INSR, phospho-INSR, IRS1, phospho-IRS1, AKT, phospho-AKT, PI3K, phospho-PI3K, GLUT2, and β-actin. Secondary HRP-conjugated antibodies appropriate for each species were used. The dilutions and catalog numbers of these antibodies are listed in **Supplementary Table 1**.

2.2 In Vitro Modeling and Cellular Assays

All cells were authenticated via STR profiling before experiments, and mycoplasma contamination tests consistently yielded negative results during cell culture. IR was modeled by exposing HepG2 cells to PA (0–400 μM) for 24 h. Based on preliminary Cell Counting Kit-8 (CCK-8) and 2-NBDG assays, 200 μM PA for 24 h was selected as

the standard IR-inducing condition, as this concentration yielded acceptable cell viability while producing a clear reduction in glucose uptake. NaB was then used to treat cells for 24 h at concentrations ranging from 0 to 3.0 mM. Based on the CCK-8 results, NaB treatment at 0.5, 1.0, and 1.5 mM showed minimal cytotoxic effects. Meanwhile, the 2-NBDG assay indicated that these concentrations produced a dose-dependent improvement in glucose uptake in PA-challenged cells. Therefore, low (0.5 mM), medium (1.0 mM), and high (1.5 mM) NaB concentrations were used in experiments. Cells in the control group were treated with the corresponding vehicle. Experimental groups were as follows: control (no treatment), IR (PA 200 μM→wash→regular medium), IR + LNaB (PA→low concentration NaB), IR + MNaB (PA→medium concentration NaB), and IR + HNaB (PA→high concentration NaB).

Cell viability was assessed using a CCK-8 assay approach. Briefly, cells grown to ~80% confluence were collected, resuspended, and adjusted to 8×10^3 cells/100 μL. A 96-well plate was seeded with 100 μL of media per well (filling edge wells with PBS) and incubated overnight. Following exposure to PA or NaB for 24 h, 100 μL of CCK-8 working solution (diluted 1:9 with complete medium) was added, and cells were incubated at 37 °C for 1 h. Absorbance at 450 nm (OD450) was then measured to quantify cell viability. PA doses for this experiment were: 0, 50, 100, 200, 300, and 400 μM; NaB doses were: 0, 0.5, 1.0, 1.5, 2.0, 2.5, and 3.0 mM. To assess glucose uptake, after 24 h of PA treatment (0–400 μM), the culture medium was replaced with glucose-free DMEM containing 50 nM insulin, and cells were incubated at 37 °C for 30 minutes. Afterward, 2-NBDG (10 μM) was added, followed by incubation at 37 °C for 1 h. Then, fluorescence was measured using a microplate reader with excitation at 485 nm and emission at 535 nm. GraphPad Prism version 10.0 (GraphPad Software, San Diego, CA, USA) was used to record all data.

2.3 Animals and Study Design

All animal experiments adhered to both institutional and national guidelines and received approval from the animal ethics committee at the Clinical Medical College of Qinghai University (P-SL-2025-024). All *in vivo* animal experiments were performed in strict accordance with the ARRIVE 2.0 guidelines. Four-week-old male C57BL/6 mice were purchased from Hangzhou Ziyuan Laboratory Animal Science and Technology Co., Ltd., and housed in a standardized controlled environment at 22 °C ± 2 °C with a 12-h light–dark cycle and unlimited access to food and water. Twenty-four mice were randomized into the following four groups (n = 6 mice/group): standard diet (SD), HFD, HFD plus low-dose NaB (HFD + LNaB), and HFD plus high-dose NaB (HFD + HNaB). For modeling, SD mice were given an SD diet for 24 weeks, while HFD mice were provided with an HFD (Research Diets, D12492, New Brunswick, NJ, USA). From weeks 16 to 24, the HFD + LNaB and HFD + HNaB groups received daily doses of NaB (Shanghai Yuanye Biotechnology Co., Ltd., S30223) at 200 and 400 mg/kg, respectively, while they continued receiving HFD.

At the end of the 24-week intervention, mice were induced with 3–4% isoflurane inhalation anesthesia and maintained with 1–2% isoflurane. Complete euthanasia was conducted via cervical dislocation after confirming loss of the pedal withdrawal reflex. Liver tissues were immediately dissected and collected after euthanasia. A portion of each sample was fixed in 4% paraformaldehyde for histological staining, and the remainder was frozen and kept at −80 °C to await further molecular assays.

2.4 In Vivo Metabolic Characterization

The HFD (D12492, Research Diets, USA) used for this study contained 60% kcal fat, 20% kcal carbohydrates, and 20% kcal protein. Mice were continuously fed a HFD for 24 weeks, with daily intragastric NaB administration (200 or 400 mg/kg) from week 16 to week 24.

Mouse body weight was monitored throughout the study period. At week 16, metabolic dysfunction in the HFD group was evaluated via oral glucose tolerance testing (OGTT), intraperitoneal insulin tolerance testing (IPITT), and serum TG measurement. Glucose or insulin were administered at body weight-adjusted doses following standardized OGTT/IPITT protocols approved by the institutional animal ethics committee (Approval No. P-SL-2025-024). Blood glucose was recorded at baseline and then at predefined time points within 120 min after dosing. The area under the curve (AUC) was computed using the trapezoidal rule. Fasting blood glucose (FBG) and 2-h postprandial blood glucose (PBG) were measured with routine glucose testing, while glycated hemoglobin (HbA1c) and fasting serum insulin levels were quantified using commercial kits. IR/sensitivity indices were calculated as follows: $\text{QUICKI} = 1/(\log_{10}[\text{fasting insulin, } \mu\text{U/mL}] + \log_{10}[\text{fasting glucose, mg/dL}])$; $\text{HOMA-IR} = (\text{FBG [mmol/L]} \times \text{fasting insulin [}\mu\text{U/mL]})/22.5$.

2.5 Histological and Cellular Staining

Lipid and glycogen alterations in HepG2 cells and murine liver tissue were examined by histological staining. After fixation, cells grown on coverslips were incubated with freshly prepared Oil Red O reagent (Solarbio) to label neutral lipid droplets, or with PAS solution (Solarbio) to detect glycogen-rich areas. Lipid droplets exhibited orange-red staining, while glycogen-positive regions appeared magenta. Nuclei were counterstained with Mayer's hematoxylin. For liver samples, paraffin-embedded sections were processed for hematoxylin and eosin (H&E) staining to assess tissue morphology and hepatic steatosis. Frozen sections were used for Oil Red O staining, whereas paraffin-embedded sections were used for PAS staining. Representative micrographs were captured using a Nikon

ECLIPSE CI microscope paired with a DS-U3 digital camera, with identical illumination, exposure, and magnification measurements applied across all experimental groups. For quantitative histomorphometric analysis, 5 randomly selected non-overlapping visual fields were captured per biological sample. All image quantification was performed by a single blinded investigator unaware of group allocation. Image segmentation and area fraction analysis for Oil Red O-positive lipid droplets and PAS-positive glycogen regions were conducted using ImageJ version 1.53e (National Institutes of Health, Bethesda, MD, USA), maintaining uniform thresholding measurements for all samples.

2.6 Biochemical Analyses

After treatment, HepG2 cells were collected, pelleted, and homogenized in 300-µL of physiological saline (five 5-s bursts at 300 W, 30-s intervals; SWE-3D homogenizer). In accordance with kit instructions, supernatants were then utilized to measure levels of glucose, TC, TG, NEFA. To ensure normalization, protein concentrations in these samples were measured via BCA assay as appropriate. A KD-810C microplate reader was used to measure absorbance. Wash steps were performed using a KD-680X washer. For intracellular glycogen quantification, cell lysates were analyzed using a Human Glycogen ELISA kit (U96-1904E; YOBIBIO, Shanghai, China) as per the manufacturer's protocol.

Serum levels of TC, TG, high-density lipoprotein cholesterol (HDL-C), and low-density lipoprotein cholesterol (LDL-C) in mice were measured using commercial assay kits (Shanghai Juchuang Pharmaceutical Technology Co., Ltd., Shanghai, China; Cat. Nos. A-1010, A-1011, A-1008, and A-1009, respectively) according to the manufacturer's instructions. Hepatic TC and TG levels were determined using commercial assay kits (Nanjing Jiancheng Bioengineering Institute, Nanjing, China; Cat. Nos. A111-1-1 and A110-1-1, respectively). Briefly, liver tissues were homogenized in physiological saline, and hepatic lipid levels were normalized to the total protein content of the corresponding tissue homogenates, as determined using the BCA method (Nanjing Jiancheng Bioengineering Institute; A045-4). Measurements of serum insulin and HbA1c levels were conducted with a Mouse Insulin/INS ELISA Kit (U96-3268E; YOBIBIO, Shanghai, China) and a Mouse HbA1c ELISA Kit (YOBIBIO, U48-8877E), respectively.

2.7 RNA-Sequencing and Pathway Analysis

RNA sequencing (RNA-seq) was performed on biological triplicate samples from the IR and IR + HNaB (1.5 mM) groups. A professional commercial mRNA sequencing service provider with a standardized quality control pipeline prepared and sequenced libraries according to standard mRNA-seq workflows. Reads underwent quality control, mapping to the human reference genome, and quantification at the gene level. Differential expression analysis was used to compare the IR and IR + HNaB groups; significance thresholds were established based on vendor/field standards (false discovery rate-adjusted $p < 0.05$). To identify pathways altered in response to NaB, KEGG pathway enrichment was performed on identified differentially expressed genes (DEGs), presenting the results using bubble/dot plots. The datasets generated during the current study are available in the [GEO] repository, [GSE325422].

2.8 RNA Isolation, Reverse Transcription, and RT-qPCR

Total RNA was extracted from cells or tissue samples using TRIzol. For cells, the culture medium was immediately removed, and cell monolayers were washed with pre-chilled PBS before lysis (1 mL of TRIzol per ~1×10^7 cells). For tissues, 1 mL of TRIzol per 100 mg of fresh tissue was used, followed by homogenization on ice. Phase separation was performed with chloroform (200 µL per 1 mL of TRIzol), followed by centrifugation at 4 °C (13,000 ×g, 15 min), precipitation with isopropanol, and washing with 75% ethanol. Pellets were air-dried and dissolved in DEPC-treated water. RNA quantity and purity were determined using a NanoDrop instrument.

Genomic DNA was removed using MonScript™ dsDNase (MRO5201; 37 °C, 2 min; 55 °C, 5 min for inactivation). For first-strand cDNA synthesis, MonScript™ RTIII Super Mix with Super NRC Mix was used (total reaction, 20 µL; 50 °C, 15 min; 85 °C, 5 min). NRC (no-RT) controls were included to exclude gDNA contamination.

RT-qPCR was performed with 2× SYBR Green qPCR Master Mix (B21202; Selleck Chemicals, Houston, TX, USA) in 20-µL reactions (cDNA, 2 µL; each primer, 0.4 µL). The primer sequences for the target genes (*SREBP1c*, *FASN*, *PGC-1α*, *PPARα*, *CPT1A*, *FOXO1*, *GSK3β*, *GS*, *PCK1*, and *G6PC1*) and the reference gene (*GAPDH*) are listed in **Supplementary Table 2**. The $2^{-\Delta\Delta Ct}$ method was used to calculate relative expression, using *GAPDH* as the internal control, and all reactions were conducted in triplicate.

2.9 Western Blotting

Cells were lysed in RIPA buffer containing PMSF. Lysates were clarified by centrifugation, and supernatant protein levels were quantified using the BCA assay. Equal amounts of protein were resolved via 10% SDS–PAGE separation followed by transfer onto PVDF or nitrocellulose membranes. Membranes were blocked with 5% nonfat milk or BSA and then incubated overnight at 4 °C with appropriate primary antibodies. After washing with tris-buffered saline with Tween 20 (TBST) or phosphate-buffered saline with Tween 20 (PBS-T), HRP-conjugated secondary antibodies were applied for 1 h at room temperature. Protein bands were detected with an ECL reagent and a chemiluminescence system. Densitometric analysis was performed using routine image quantification software. Phosphorylated target protein levels were quantified relative to their

matched total protein levels, with β-actin included as a loading control.

2.10 Analysis of Inflammatory Activity

After NaB treatment, HepG2 cell lysates were collected and homogenized. Intracellular TNF-α, IL-6, IL-1β, and MCP-1 concentrations were determined using corresponding commercial ELISA kits in accordance with manufacturer's instructions. All cytokine levels were normalized to total cellular protein levels as detected by BCA assay, presenting results as pg/mg total protein. At the end of a 24-week intervention period, murine peripheral blood was collected to separate serum. Liver tissues were homogenized in pre-cooled lysis buffer to measure hepatic cytokine levels. Serum TNF-α, IL-6, IL-1β, MCP-1 (units: pg/mL) and hepatic TNF-α, IL-6 (units: pg/mg total protein) were quantified with appropriate ELISA kits. Total RNA extracted from liver tissue was reverse-transcribed into cDNA. Relative mRNA expression of the macrophage marker F4/80 was detected by RT-qPCR, quantifying relative expression using the $2^{-\Delta\Delta Ct}$ method with *GAPDH* as internal reference for normalization. All ELISA and RT-qPCR experiments were performed with three technical replicates for each biological sample.

2.11 Statistical Analyses

Results are presented as mean ± standard deviation. Normality of data distribution and homogeneity of variance were assessed using the Shapiro–Wilk test and Levene's test prior to statistical comparison. All *in vitro* experiments were replicated at least three times independently, with three technical replicates for each experiment. *In vivo* experiments utilized six mice per experimental group, with no a priori power calculation performed to define sample size. Unpaired two-tailed Student's *t*-tests were applied for two-group comparisons when data met the assumptions of normality and equal variance. For multi-group comparisons, one-way analyses of variance (ANOVAs) were implemented, followed by Tukey's honest significant difference (HSD) post-hoc testing with correction for multiple pairwise comparisons to control type I error. All statistical tests were two-sided, with $p < 0.05$ as the significance threshold. Full details of replicate numbers (n), statistical testing approaches, and exact *p*-values are reported in figure legends and the main text where applicable.

3. Results

3.1 NaB Reduces PA-Induced Lipid Accumulation

To generate an *in vitro* model of IR, HepG2 cells were treated with different concentrations of PA. Exposure to 200 μM PA for 24 h markedly impaired glucose uptake without causing excessive loss of cell viability, such that this concentration was selected for subsequent experiments (Fig. 1A,B). Analysis of NaB-associated cytotoxicity revealed that cell viability remained largely unchanged after treatment with 0.5–1.5 mM NaB, and these concentrations were therefore selected for further evaluation in intervention experiments (Fig. 1C).

After establishing the PA-induced IR model and NaB treatment conditions, lipid metabolic changes were next assessed. In PA-exposed HepG2 cells, NaB visibly reduced Oil Red O-positive lipid droplet accumulation (Fig. 1D), with quantification confirming that the magnitude of this response was stronger at an NaB concentration of 1.0 and 1.5 mM relative to 0.5 mM (Fig. 1E).

Consistently, biochemical assays revealed that NaB decreased intracellular TG, TC, and NEFA levels. Together, these findings indicate that NaB alleviates PA-induced lipid metabolic abnormalities in HepG2 cells under conditions of IR model establishment without inducing any overt cytotoxicity (Fig. 1F–H).

3.2 NaB Remediates Cellular Glucose Processing and Glycogen Storage

PAS staining first revealed that glycogen deposition was markedly reduced in PA-treated HepG2 cells compared with control cells, indicating the impairment of glucose utilization and storage under IR conditions (Fig. 2A). Image-based quantification yielded similar results and demonstrated that NaB gradually restored PAS staining intensity in a dose-dependent manner (Fig. 2B).

We further evaluated cellular glucose uptake using 2-NBDG staining. PA-treated HepG2 cells showed a clear reduction in 2-NBDG fluorescence, whereas NaB restored this fluorescent signal, particularly at higher concentrations (Fig. 2C). Measurement of intracellular free glucose showed the opposite pattern, with free glucose accumulation in PA-treated cells that declined following NaB intervention (Fig. 2D). This result indicates that PA exposure disrupts both glucose uptake and downstream intracellular glucose utilization.

In line with these staining results, glycogen ELISAs showed increases in glycogen content after NaB treatment, particularly following exposure to higher doses (Fig. 2E). Overall, NaB stimulation shifted glucose metabolism in insulin-resistant HepG2 cells toward greater glucose uptake, lower levels of intracellular glucose retention, and enhanced glycogen storage.

3.3 Transcriptomic Profiling Reveals the Coordinated NaB-Induced Reprogramming of Hepatic Glycolipid Metabolism

To systematically characterize transcriptional changes in response to NaB under conditions of PA-induced hepatic IR, we performed mRNA sequencing across five experimental groups (Control, IR model, IR + 0.5 mM NaB, IR + 1.0 mM NaB, IR + 1.5 mM NaB), with three biological replicates per cohort. All multi-dimensional transcriptomic datasets were integrated into a single composite Supplementary Figure (**Supplementary Fig. 1**).

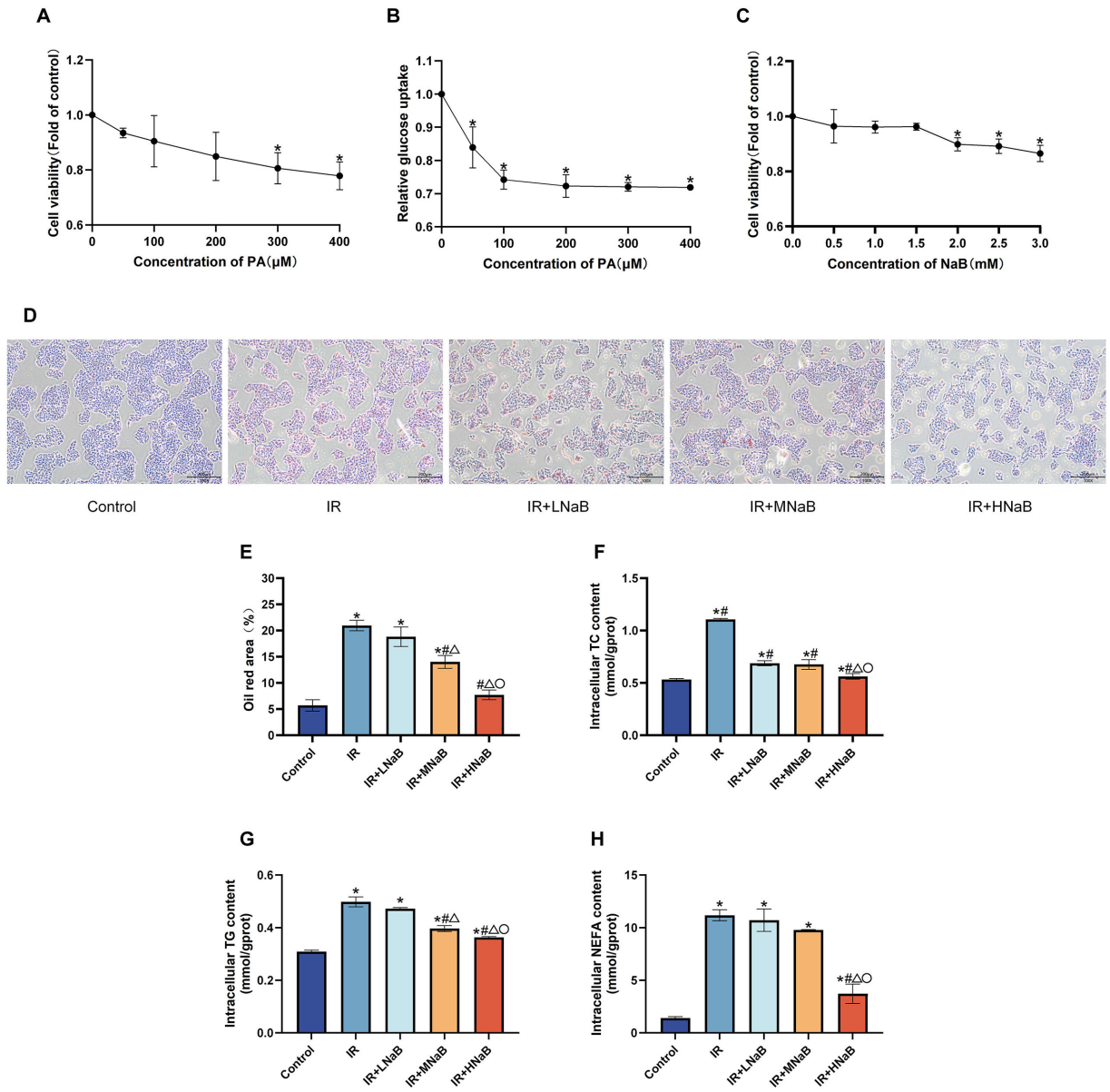

Fig. 1. Sodium butyrate (NaB) alleviates intracellular lipid accumulation in palmitate (PA)-induced insulin-resistant HepG2 hepatocytes. To model insulin resistance (IR) *in vitro*, HepG2 cells were treated with 200 μM PA for 24 h; intervention groups received 0.5 mM low NaB (IR + LNaB), 1.0 mM medium NaB (IR + MNaB), or 1.5 mM high NaB (IR + HNaB) for an additional 24 h after PA stimulation. (A) CCK-8 analysis of the viability of HepG2 cells incubated with a range of PA concentrations (0, 50, 100, 200, 300, 400 μM) for 24 h, n = 3 independent biological replicates. (B) Quantitative analysis of 2-NBDG fluorescence as a measure of relative glucose uptake capacity after exposure to a range of PA concentrations (0–400 μM), n = 3. (C) CCK-8 analysis of the viability of HepG2 cells treated with a range of NaB concentrations (0–3.0 mM) in the absence of PA pretreatment, n = 3. (D) Representative microscopic images of Oil Red O staining for intracellular neutral lipid droplets in the Control, IR, IR + LNaB, IR + MNaB, and IR + HNaB groups under identical magnification. Lipid droplets are stained orange-red. Scale bar: 200 μm (100×). (E) Quantitative analysis of Oil Red O-positive lipid area percentages for the images in panel D, n = 3. (F) Biochemical analysis of intracellular total cholesterol (TC) levels normalized to total cellular protein across all experimental groups, n = 3. (G) Biochemical analysis of intracellular triglyceride (TG) levels normalized to total cellular protein across all experimental groups, n = 3. (H) Biochemical analysis of intracellular non-esterified fatty acids (NEFA) levels normalized to total cellular protein across all experimental groups, n = 3. All data are presented as mean ± standard deviation. *$p < 0.05$ vs. Control group; #$p < 0.05$ vs. IR group; △$p < 0.05$ vs. IR + LNaB group; ○$p < 0.05$ vs. IR + MNaB group. Abbreviations: IR, insulin resistance; L/M/HNaB, low/medium/high sodium butyrate.

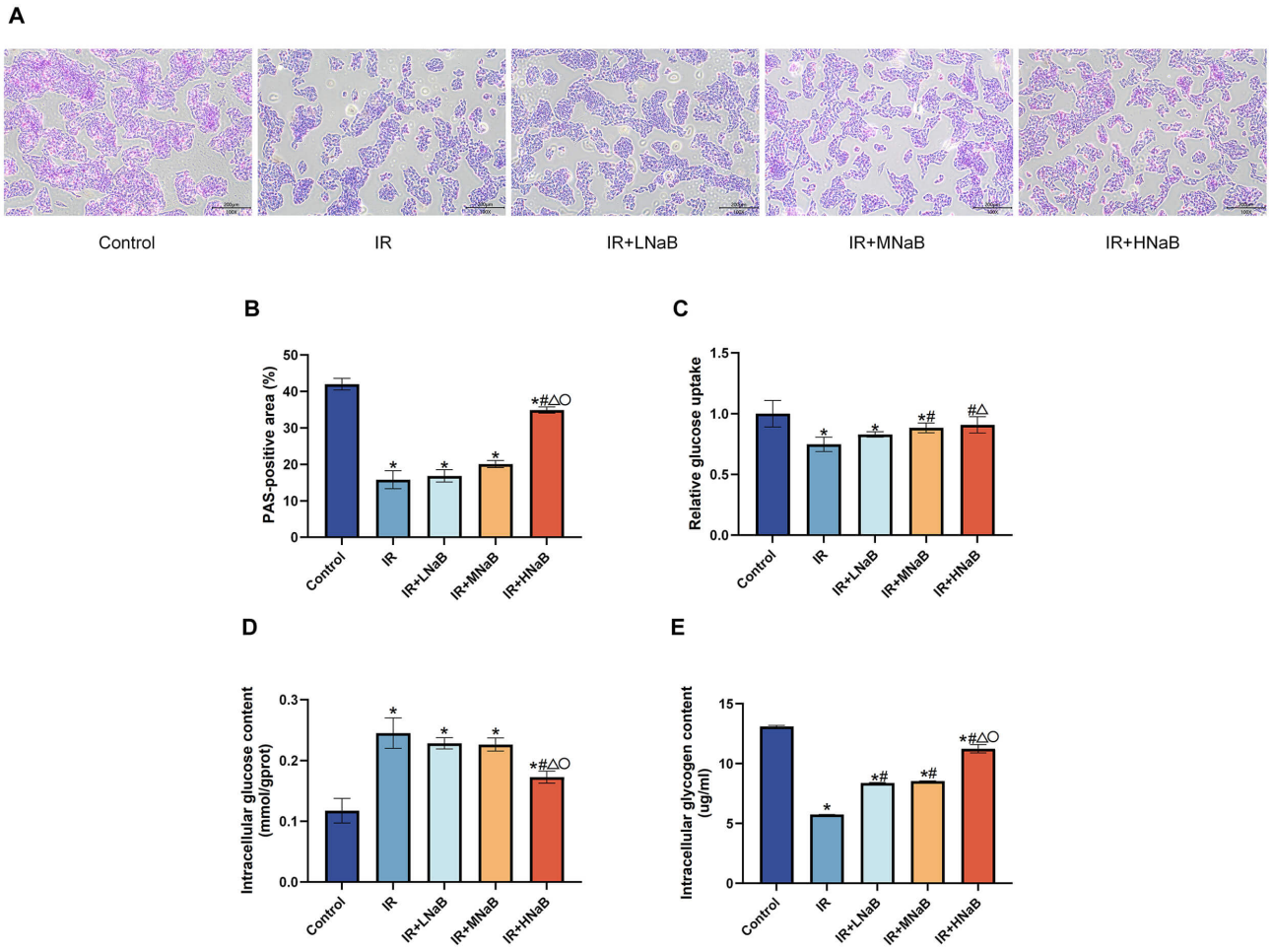

Fig. 2. NaB promotes glucose uptake and glycogen accumulation in PA-induced insulin-resistant HepG2 cells. (A) Representative periodic acid–Schiff (PAS) staining micrographs showing intracellular glycogen deposition in each group; glycogen-rich regions appear in magenta, while cell nuclei are counterstained with hematoxylin. All images are shown under identical magnification. Scale bar: 200 μm (100×). (B) Quantitative analysis of the PAS-positive glycogen area percentage corresponding to images shown in (A), n = 3 biological replicates. (C) Relative cellular glucose uptake as quantified using the 2-NBDG fluorescent probe, n = 6 replicates per group. (D) Biochemical detection of free intracellular glucose levels normalized to total cellular protein, n = 3. (E) Intracellular glycogen concentration measured by ELISA using approximately 1.5×10^6 cells per sample, expressed as μg/mL, n = 3. Data are expressed as mean ± standard deviation. *$p < 0.05$ vs. Control; #$p < 0.05$ vs. IR; △$p < 0.05$ vs. IR + LNaB; ○$p < 0.05$ vs. IR + MNaB.

Principal component analysis (PCA) was first implemented based on normalized FPKM gene expression values to evaluate sample reproducibility and intergroup transcriptional divergence (**Supplementary Fig. 1A**, 2D-PCA; **Supplementary Fig. 1B**, 3D-PCA). PC1 captured 80.35% of total transcriptional variance, while PC2 and PC3 accounted for 10.48% and 3.25% of variance, respectively. Biological replicates within each group exhibited tight clustering, demonstrating reliable experimental consistency. The IR group was fully separated from untreated Control samples, confirming that PA exposure triggered profound transcriptional changes in hepatocytes. Notably, NaB-treated samples shifted progressively toward the Control cluster along the PC1 axis in a dose-dependent manner, confirming the ability of NaB to reverse PA-induced transcriptomic dysregulation in a concentration-responsive manner.

Differentially expressed genes (DEGs) were screened with uniform cutoffs of *p*adj < 0.05 and $|\log_2 FC| > 1$. A total of 8732 DEGs were identified when comparing the IR + HNaB and IR groups, including 6075 significantly upregulated transcripts and 2657 significantly downregulated transcripts. The differential expression patterns of these DEGs were visualized with a volcano plot (**Supplementary Fig. 1C**). Further analysis revealed that canonical lipogenic genes (*SREBF1c*, *FASN*) and gluconeogenic mediators (*FOXO1*, *PCK1*) were downregulated following high-dose NaB treatment, whereas genes involved in fatty acid oxidation (*PPARA*, *CPT1A*) and insulin signal transduction (*IRS1*, *GYS1*) were upregulated. A hierarchical

clustering heatmap analysis of all DEGs further delineated distinct transcriptional signatures across all five groups (**Supplementary Fig. 1D**). Notably, the IR group exhibited a distinct expression profile characterized by enhanced lipogenic/gluconeogenic programs and downregulation of insulin-sensitizing metabolic transcripts, whereas dose-dependent NaB treatment gradually restored a transcriptional pattern resembling that of the control group. A full list of representative glycolipid metabolism-related DEGs with corresponding $\log_2$FC and padj values is presented in **Supplementary Table 3** to provide further quantitative support of the differential expression of these core functional genes.

Pathway-level functional enrichment analysis was next conducted using KEGG pathway enrichment (**Supplementary Fig. 1E**) and alternative splicing (AS) enrichment analysis (**Supplementary Fig. 1F**). KEGG enrichment analysis identified multiple significantly enriched pathways, with the PPAR signaling pathway among the prominent metabolism-related pathways associated with NaB treatment. This finding was consistent with the observed transcriptional changes in genes involved in lipid metabolism. In parallel, AS enrichment analysis further identified additional enriched metabolic and signaling pathways, complementing the KEGG-based pathway analysis.

To systematically explore upstream transcriptional regulatory mechanisms not captured by the initial KEGG analysis, we performed transcription factor (TF) classification and TF-target regulatory network analysis (**Supplementary Fig. 1G**). All differentially active TF families were presented in a pie chart, and a Sankey diagram was used to visualize hierarchical regulatory cascades linking TF families, core metabolic TFs, and downstream lipid/glucose-related target genes. The lipogenic and gluconeogenic master upstream regulators *SREBF1c* and *FOXO1* were significantly downregulated upon NaB treatment, whereas TFs that promote oxidative metabolism, such as *PPARA*, *SIRT1*, and *CREB3L*, were notably upregulated, consistent with the quantification of TF gene expression summarized in **Supplementary Table 3**. We further constructed a protein-protein interaction (PPI) network using the top 300 most variable DEGs (**Supplementary Fig. 1H**), leading to the identification of *PPARA*, *SIRT1*, *AMPKα*, and *FOXO1* as central hub regulators bridging the AMPK and PI3K/AKT signaling axes. Collectively, this multi-layered transcriptomic analysis offers a systematic overview of this regulatory axis, demonstrating that NaB remodels hepatic lipid and glucose transcriptional networks through the bidirectional modulation of core metabolic TFs to alleviate PA-induced hepatic IR.

3.4 NaB Activates AMPK Signaling and Rebalances Lipid Metabolism-Related Gene Expression

The next series of experiments was designed to explore the NaB-mediated activation of the GPR43/CaMKK2/AMPK/SIRT1 axis and the rebalancing of lipid metabolism-related programs in insulin-resistant HepG2 cells. Western blotting revealed that IR conditions suppressed GPR43 and p-AMPKα^{Thr172} levels, in addition to reducing SIRT1 expression and abnormally increasing p-CaMKK2^{Ser495} levels. NaB reversed these changes in a dose-dependent manner, increasing GPR43 levels and restoring p-AMPKα^{Thr172} and SIRT1 levels toward those observed in the control group, while also normalizing p-CaMKK2^{Ser495} levels (Fig. 3A–D). These findings suggest that NaB may alleviate the inhibition of AMPK signaling by reducing the inhibitory phosphorylation of CaMKK2 at Ser495, thereby promoting activation of the AMPK signaling axis. In line with these results, RT-qPCR analysis revealed the ability of IR conditions to upregulate the lipogenic drivers *SREBP1c* and *FASN*, while NaB reversed these changes in a dose-dependent fashion (**Supplementary Fig. 2A,B**). In contrast, transcripts supporting fatty acid oxidation and mitochondrial biogenesis (*PGC-1α*, *PPARα*, and *CPT1A*) were repressed by IR and robustly rescued by NaB, with the high dose frequently outperforming the control (**Supplementary Fig. 2C–E**). These findings link AMPK pathway restoration to a coordinated shift away from lipid synthesis and toward oxidative lipid metabolism.

3.5 NaB Strengthens Insulin Signaling via the PI3K/AKT Pathway and Preserves Receptor Fidelity

The next experiments explore the ability of NaB to restore downstream insulin signaling through the PI3K/AKT pathway and to improve the regulation of glucose metabolism. IR was found to be associated with the impairment of multiple nodes of the insulin cascade, as levels of p-INSR^{Tyr1150}, p-IRS1^{Tyr895}, p-PI3K^{Tyr458}, and p-AKT^{Ser473} were all reduced under IR conditions, and GLUT2 expression levels were decreased. NaB did not detectably restore INSR phosphorylation (Fig. 3E); however, it significantly increased p-IRS1^{Tyr895} levels (which returned to control levels in response to 1.0–1.5 mM NaB), dose-dependently increased p-PI3K^{Tyr458} and p-AKT^{Ser473} levels, and elevated GLUT2 protein expression (Fig. 3F–I). Even in the absence of measurable changes in receptor phosphorylation, NaB thus enhanced downstream signal transduction and glucose transporter availability, with these effects being associated with improved insulin sensitivity.

Consistent with the protein signaling data, IR was associated with the upregulation of gluconeogenic and catabolic driver genes (*FOXO1*, *PCK1*, and *G6PC1*) and the glycogen-antagonizing kinase *GSK3β*, while suppressing *GS*. NaB dose-dependently reduced *FOXO1*, *PCK1*, *G6PC1*, and *GSK3β* mRNA levels while promoting *GS*

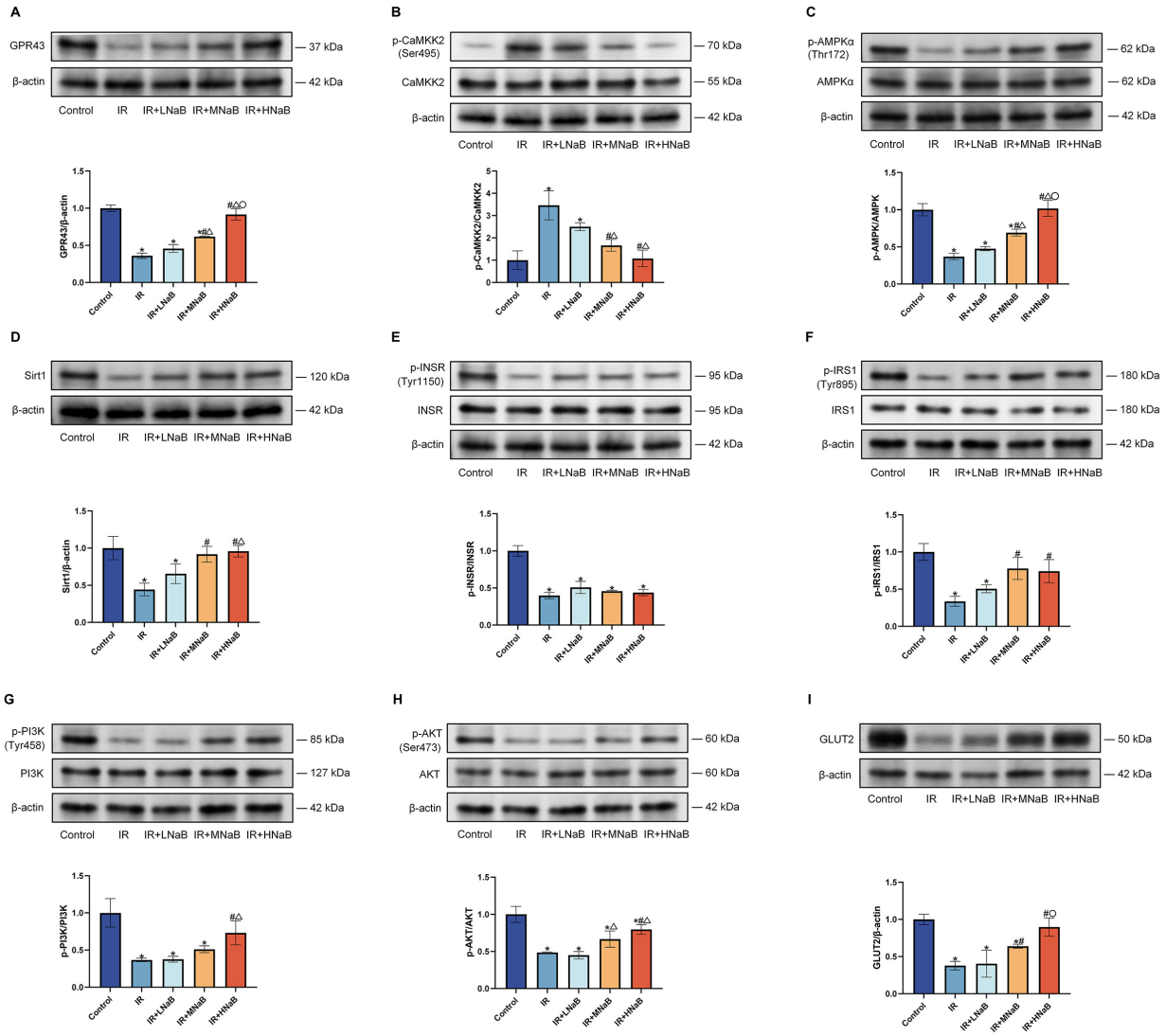

Fig. 3. Sodium butyrate (NaB) activates both the AMPK and PI3K/AKT signaling pathways in insulin-resistant HepG2 cells. (A) Immunoblot bands and corresponding densitometric quantification of GPR43 protein expression in each experimental group. (B) Immunoblot bands and corresponding densitometric quantification of total CaMKK2 and phosphorylated CaMKK2 (Ser495, p-CaMKK2); p-CaMKK2 signal was normalized to total CaMKK2. (C) Immunoblot bands and corresponding densitometric quantification of total AMPKα and phosphorylated AMPKα (Thr172, p-AMPKα); p-AMPKα signal was normalized to total AMPKα. (D) Immunoblot bands and corresponding densitometric quantification of SIRT1 protein expression. (E) Immunoblot bands and corresponding densitometric quantification of total insulin receptor (INSR) and phosphorylated INSR (Tyr1150, p-INSR); p-INSR signal was normalized to total INSR. (F) Immunoblot bands and corresponding densitometric quantification of total insulin receptor substrate 1 (IRS1) and phosphorylated IRS1 (Tyr895, p-IRS1); p-IRS1 signal was normalized to total IRS1. (G) Immunoblot bands and corresponding densitometric quantification of total PI3K and phosphorylated PI3K (Tyr458, p-PI3K); p-PI3K was normalized to total PI3K. (H) Immunoblot bands and corresponding densitometric quantification of total AKT and phosphorylated AKT (Ser473, p-AKT); p-AKT was normalized to total AKT. (I) Immunoblot bands and corresponding densitometric quantification of glucose transporter 2 (GLUT2) protein expression. All quantitative data are shown as mean ± standard deviation. *$p < 0.05$ vs. Control group; #$p < 0.05$ vs. IR group; △$p < 0.05$ vs. IR + LNaB group; ○$p < 0.05$ vs. IR + MNaB group. Abbreviations: p-, phosphorylated protein.

upregulation (**Supplementary Fig. 2F–J**), establishing a mechanistic link between the restoration of AKT signaling and the observed improvements in glycogen content and glucose tolerance. Thus, NaB improved glucose metabolic control at both the signaling and effector levels, providing a mechanistic basis for the observed increases in glucose uptake and glycogen storage in treated cells.

3.6 HFD Conditions Induce a MASLD/IR-Like Phenotype In Vivo

After 16 weeks of HFD feeding, mice developed a robust metabolic phenotype consistent with MASLD and systemic IR. Compared with SD controls, HFD-fed mice showed increased body weight and elevated serum TG levels, indicating the successful induction of diet-related metabolic disturbance (Fig. 4A,B; $p < 0.05$). HFD feeding was also associated with impaired glycemic control, as reflected by increased fasting and 2-h postprandial blood glucose levels (Fig. 4C,D; $p < 0.05$). Dynamic metabolic testing further confirmed systemic glucose intolerance and IR, with HFD mice exhibiting higher OGTT and IPITT AUC values relative to controls (Fig. 4E–H; $p < 0.05$). HFD-fed mice developed both hepatic lipid accumulation and impaired glucose metabolism, making this model appropriate for testing the effects of NaB on steatosis and IR-related changes.

3.7 NaB Attenuates Hepatic Steatosis and Dyslipidemia in MASLD Mice

NaB alleviated hepatic steatosis in HFD-fed mice as evidenced by consistent improvements across morphological and biochemical endpoints. NaB treatment from week 16 to week 24 limited HFD-related body weight gain, especially at 400 mg/kg (Fig. 5A). In the liver, both TG and TC levels were reduced after NaB administration (Fig. 5B,C). H&E-stained sections showed fewer lipid vacuoles, and Oil Red O staining revealed weaker neutral lipid deposition in the NaB-treated groups. Image-based quantification further indicated that these histological changes were more pronounced with the higher NaB dose (Fig. 5D–F). Systemically, NaB reduced serum TC, TG, and LDL-C levels while increasing HDL-C levels (Fig. 5G–J). These results indicate that NaB alleviated both hepatic steatosis and systemic dyslipidemia in HFD-fed mice, which is consistent with the *in vitro* finding that NaB suppressed lipogenic signaling and promoted lipid oxidation-related programs.

3.8 NaB Improves Whole-Body Insulin Sensitivity and Restores Hepatic Glycogen In Vivo

We next examined the ability of NaB to remediate glucose metabolic dysfunction and IR *in vivo*, ultimately revealing that NaB administration improved whole-body glucose homeostasis and restored hepatic glycogen storage in HFD-fed mice. Specifically, NaB reduced FBG and PBG levels and improved glucose tolerance (reduced OGTT AUC) while improving insulin sensitivity (lower IPITT AUC), with the 400 mg/kg dose generally performing better than 200 mg/kg (Fig. 6A–F). PAS staining revealed the recovery of hepatic glycogen concentrations, which returned to levels similar to those of the control group at the higher dose level, as confirmed through quantitative image analysis (Fig. 6G,H). Biochemical indices were consistent with these functional improvements, as NaB treatment decreased HbA1c levels, lowered fasting insulin levels, reduced HOMA-IR values, and increased QUICKI (Fig. 6I–L). Together, these findings indicate that NaB improved both hepatic glucose storage and whole-body insulin sensitivity in HFD-fed mice, which is in line with the *in vitro* observation that NaB enhanced PI3K/AKT-related insulin signaling and promoted glycogen synthesis-associated molecular changes.

In both *in vitro* and *in vivo* experiments, NaB alleviated a range of metabolic disturbances, including excessive lipid accumulation, impaired glucose uptake, reduced glycogen deposition, abnormal serum metabolic indices, and decreased insulin sensitivity. Mechanistically, NaB treatment was linked to activation of the GPR43/CaMKK2/AMPK/SIRT1 pathway, weaker lipogenic activity, increased fatty acid oxidation, recovery of IRS1/PI3K/AKT/GLUT2 signaling, and reduced gluconeogenic marker expression. Rather than pointing to a single downstream event, these results describe a broader regulatory pattern involving both lipid and glucose metabolism. This integrated mechanism is summarized in Fig. 7.

3.9 NaB Inhibits Systemic and Hepatic Inflammatory Activity

Excessive lipid accumulation triggers inflammatory cascade activity in hepatocytes. We therefore measured intracellular pro-inflammatory cytokine levels to evaluate the anti-inflammatory capacity of NaB (**Supplementary Table 4**). Compared with the Control group, PA treatment dramatically elevated intracellular TNF-α, IL-6, IL-1β and MCP-1 levels. After NaB administration, the concentrations of four pro-inflammatory mediators decreased in a dose-dependent manner such that the IR + LNaB group exhibited significantly lower cytokine levels than the IR group, while the IR + HNaB group showed further reductions compared with the IR + LNaB group. High-dose 1.5 mM NaB treatment led to the restoration of inflammatory factor levels to near the baseline levels observed in normal hepatocytes, demonstrating that NaB effectively suppresses lipotoxicity-induced hepatocyte inflammation in a concentration-dependent manner.

We further detected circulating and hepatic inflammatory factors, as well as the mRNA expression of the macrophage marker F4/80 in animal models (Table 1). After 24 weeks of HFD feeding, serum and hepatic TNF-α, IL-6, IL-1β, and MCP-1 levels were markedly increased relative to the SD group (all $*p < 0.05$). Relative hepatic F4/80 expression was upregulated 3.72-fold compared to normal control mice, consistent with extensive macrophage recruitment and severe hepatic inflammatory infiltration in MASLD mice. Treatment with NaB for 8 weeks significantly reversed this excessive inflammation. Both low-dose (200 mg/kg) and high-dose (400 mg/kg) NaB clearly decreased serum and hepatic pro-inflammatory cytokine levels compared with the HFD group ($\#p < 0.05$). More-

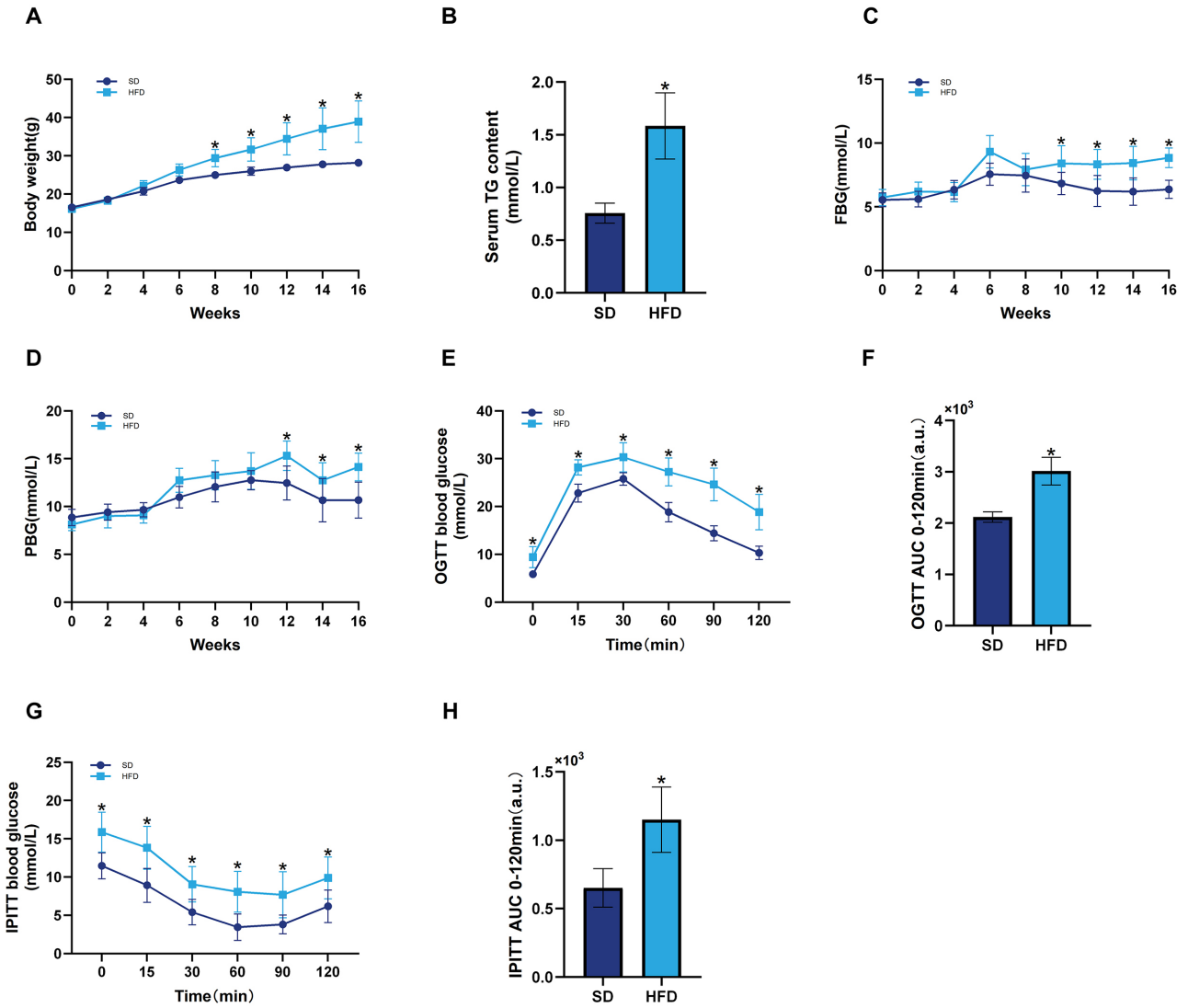

Fig. 4. Establishment of a diet-induced MASLD mouse model. (A) Dynamic body weight curve recorded every 2 weeks from week 0 to week 16 in the SD and HFD cohorts. (B) Serum triglyceride (TG) concentration as detected using a commercial kit at week 16, n = 6 per group. (C) Longitudinal fasting blood glucose (FBG) levels measured biweekly throughout the 16-week feeding period. (D) Longitudinal 2-hour postprandial blood glucose (PBG) levels measured biweekly throughout the 16-week feeding period. (E) Dynamic blood glucose curve for the oral glucose tolerance test (OGTT) within 0–120 min after glucose gavage at week 16. (F) Calculated area under the curve (AUC) for the OGTT glucose curve in (E). (G) Dynamic blood glucose curve for intraperitoneal insulin tolerance test (IPITT) within 0–120 min after insulin injection at week 16. (H) Calculated AUC for the IPITT glucose curve in (G). Data represent mean ± standard deviation. *$p < 0.05$ vs. SD group.

over, the HFD + HNaB group exhibited superior anti-inflammatory and anti-macrophage infiltration effects as compared to the HFD + LNaB group ($\triangle p < 0.05$). The F4/80 mRNA level was notably downregulated in response to high-dose NaB, suggesting that NaB inhibits macrophage accumulation in the liver, thereby alleviating hepatic inflammatory injury in MASLD.

4. Discussion

There are several major findings from this study to highlight. First, NaB reduced changes consistent with hepatic steatosis in both PA-treated HepG2 cells and HFD-fed mice, as reflected by reduced lipid accumulation and improved lipid-related biochemical indices. Second, NaB was associated with improvements in IR-related phenotypes, including glucose uptake, glycogen storage, glucose tolerance, and insulin sensitivity. Third, these metabolic changes were accompanied by the recovery of AMPK and PI3K/AKT signaling, together with transcriptional changes consistent with reduced lipogenesis, enhanced fatty acid oxidation, lower gluconeogenic drive, and increased glycogen synthesis. In addition to these effects on glycolipid

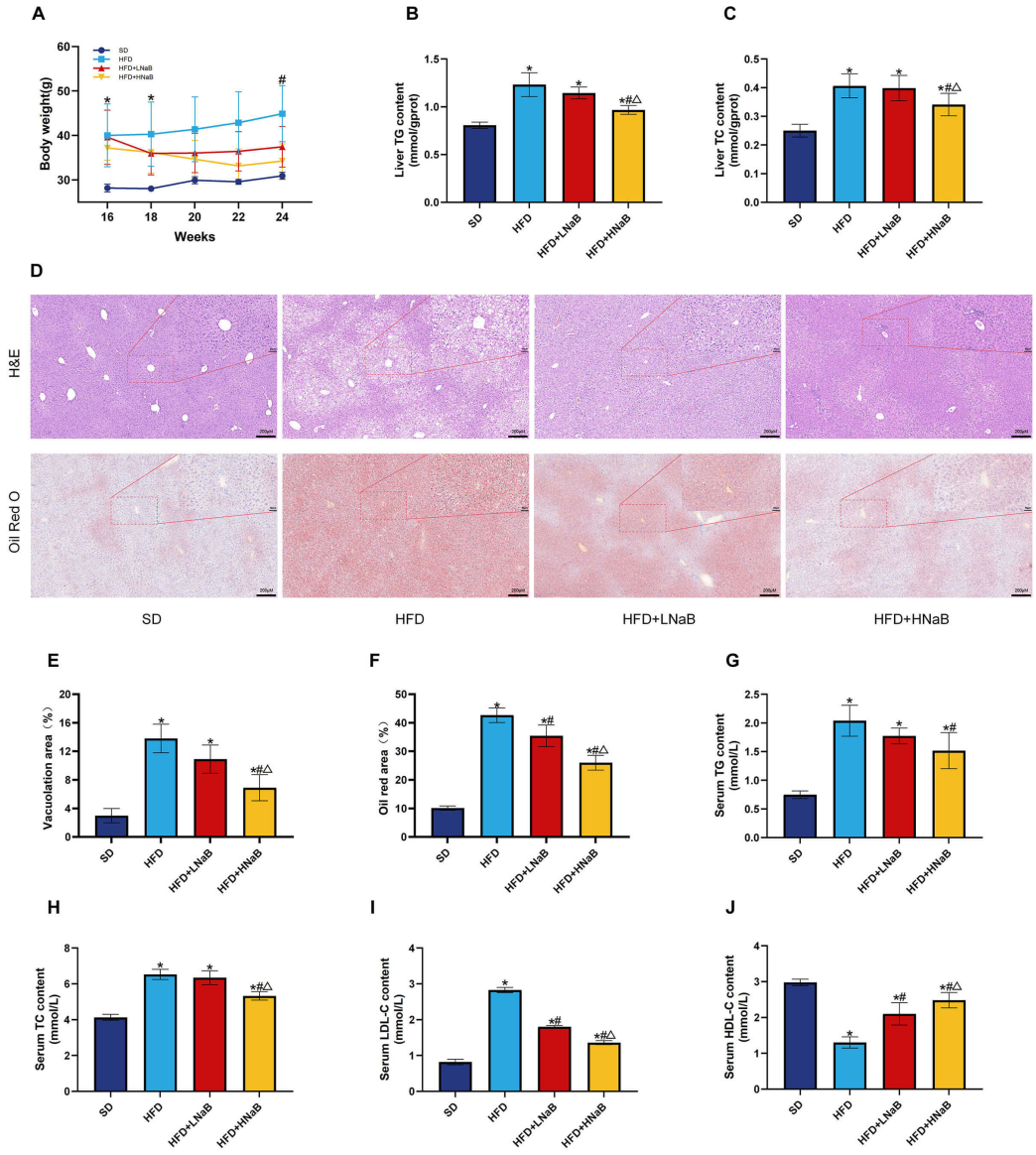

Fig. 5. Sodium butyrate (NaB) attenuates hepatic steatosis in MASLD mice. (A) Body weight tracking curve from week 16 to week 24 during the NaB treatment intervention period. (B) Biochemical quantification of hepatic triglyceride (TG) content normalized to total liver protein at the end of intervention. (C) Biochemical quantification of hepatic total cholesterol (TC) content normalized to total liver protein at the end of intervention. (D) Representative liver tissue histology slides; Upper row: hematoxylin and eosin (H&E) staining showing hepatic lipid vacuoles; Lower row: frozen section Oil Red O staining showing neutral lipid deposition. All slides are shown at the same level of magnification. Main image scale bar = 200 μm; inset (upper right, magnified) scale bar = 50 μm. (E) Quantitative analysis of hepatic lipid vacuole area percentages from H&E-stained liver sections in (D), n = 3 tissue samples per group. (F) Quantitative analysis of Oil Red O-positive lipid area percentages from frozen liver sections in (D), n = 3 tissue samples per group. (G) Serum triglyceride (TG) concentration as measured after the 8-week intervention period, n = 6. (H) Serum total cholesterol (TC) concentration as measured after the 8-week intervention period, n = 6. (I) Serum low-density lipoprotein cholesterol (LDL-C) concentration as measured after the 8-week intervention period, n = 6. (J) Serum high-density lipoprotein cholesterol (HDL-C) concentration as measured after the 8-week intervention period, n = 6. All data are mean ± standard deviation. *$p < 0.05$ vs. SD; #$p < 0.05$ vs. HFD; △$p < 0.05$ vs. HFD + LNaB.

homeostasis, quantitative analysis of inflammatory factors (**Supplementary Table 4**, Table 1) confirmed that NaB alleviated MASLD-related low-grade inflammation by reducing TNF-α, IL-6, IL-1β, and MCP-1 secretion while also reducing hepatic macrophage infiltration, highlighting a link between AMPK/PI3K/AKT pathway activation and the improvement of immuno-metabolic status. Together, these correlative findings indicate that NaB treatment co-

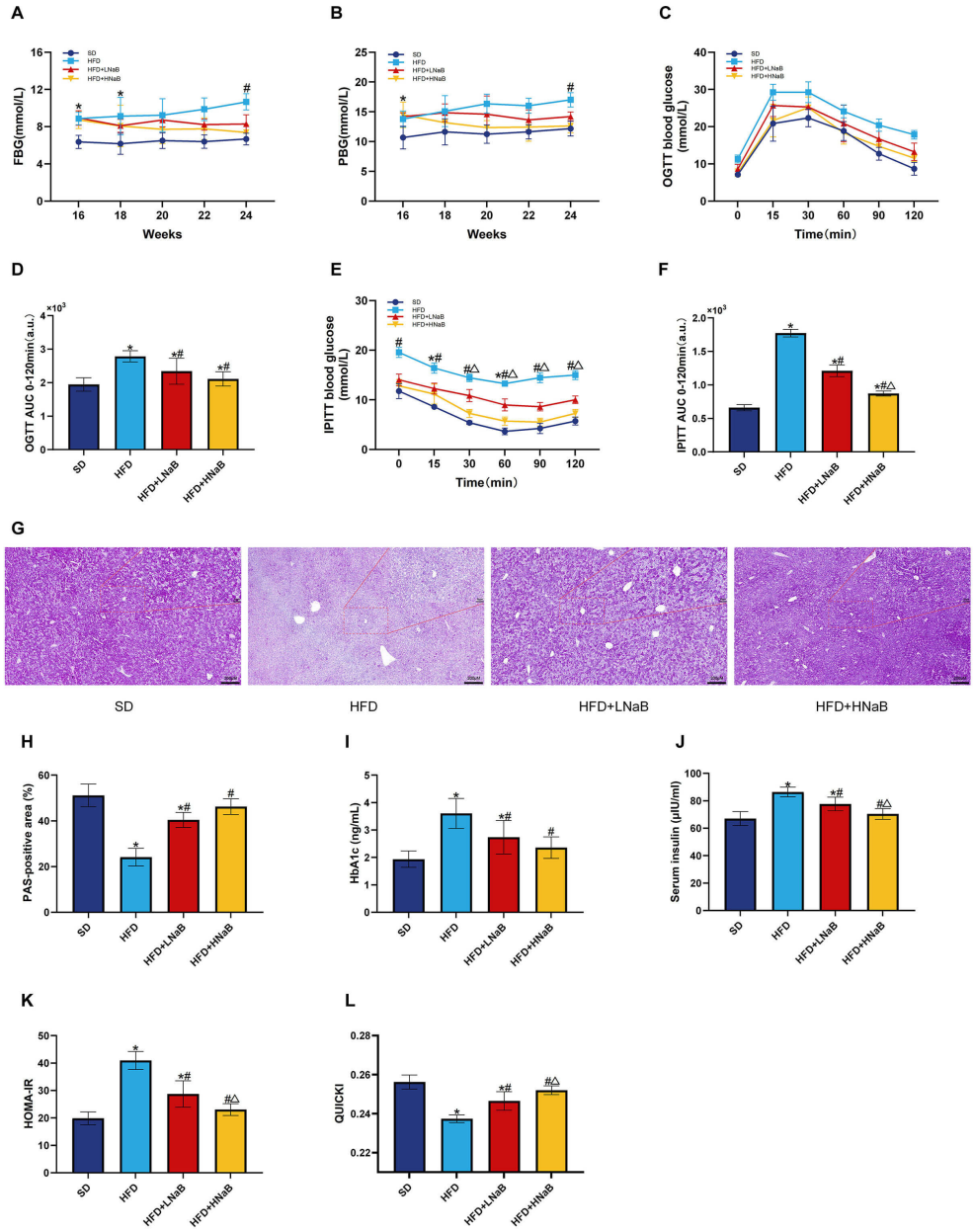

Fig. 6. Sodium butyrate (NaB) improves systemic insulin resistance and hepatic glycogen accumulation in MASLD mice. (A) Biweekly fasting blood glucose (FBG) levels recorded from week 16 to week 24 during the intervention period. (B) Biweekly 2-h postprandial blood glucose (PBG) levels recorded from week 16 to week 24 during the intervention period. (C) Dynamic OGTT blood glucose curve at week 24 when the intervention period was complete. (D) Calculated AUC for the OGTT glucose curve shown in (C). (E) Dynamic IPITT blood glucose curve at week 24 when the intervention period was complete. (F) Calculated AUC for the IPITT glucose curve shown in (E). (G) Glycogen detection in representative PAS staining images for paraffin-embedded liver tissues; magenta signal indicates glycogen enrichment. All images are shown under identical magnification. Main image scale bar = 200 μm; inset (upper right, magnified) scale bar = 50 μm. (H) Quantification of PAS-positive glycogen area percentage from liver sections in (G), n = 6 liver samples per group. (I) Serum glycated hemoglobin (HbA1c) concentration as measured by ELISA, n = 6. (J) Fasting serum insulin concentration as measured by ELISA, n = 6. (K) Homeostasis model assessment of insulin resistance (HOMA-IR) values calculated using FBG and fasting insulin values. (L) Quantitative insulin sensitivity check index (QUICKI) values calculated using FBG and fasting insulin values. All quantitative data are presented as mean ± standard deviation. *$p < 0.05$ vs. SD; #$p < 0.05$ vs. HFD; △$p < 0.05$ vs. HFD + LNaB. The HOMA-IR and QUICKI formulas are defined in the Materials and Methods.

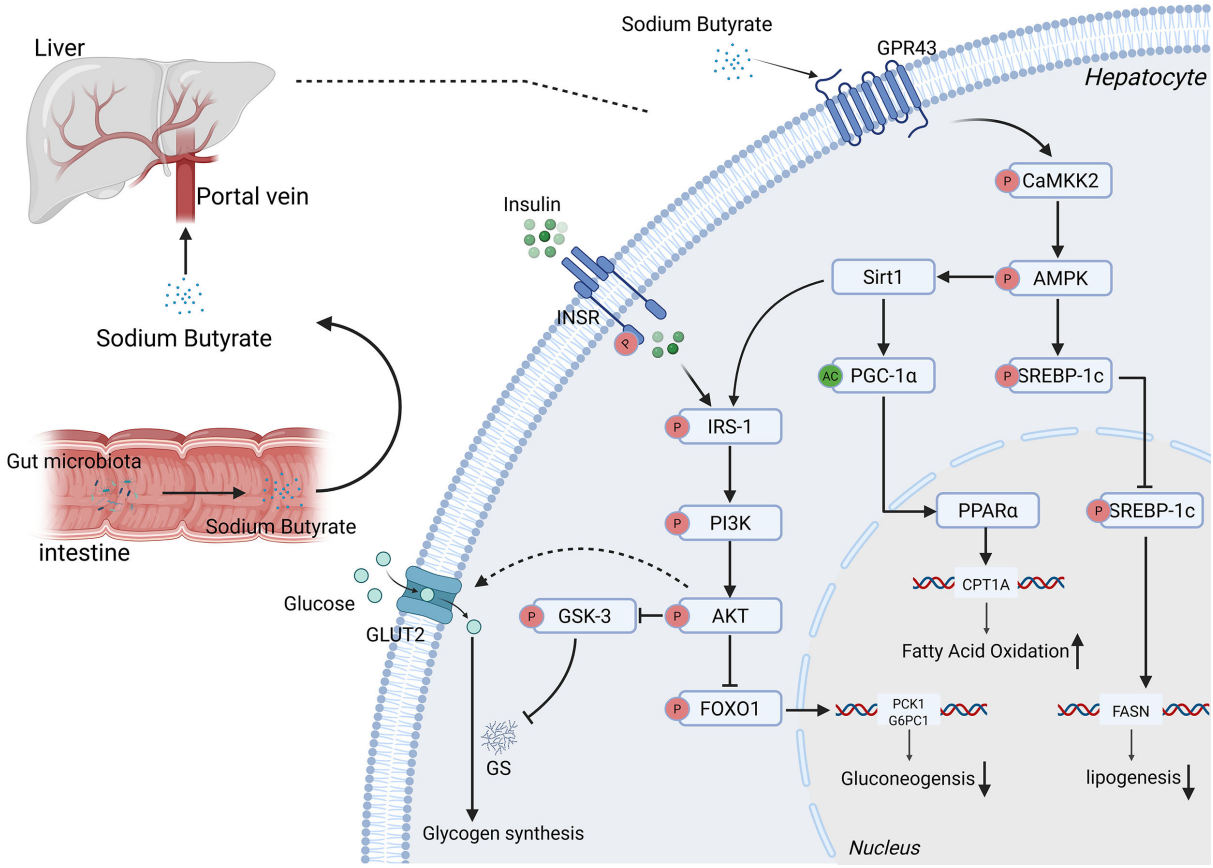

Fig. 7. Schematic working model illustrating the proposed sodium butyrate (NaB)-coordinated regulation of hepatic AMPK and PI3K/AKT signaling to alleviate MASLD-associated hepatic steatosis and insulin resistance. Gut microbiota ferment dietary fiber to generate NaB, which enters portal circulation and acts on the hepatocyte membrane GPR43 receptor. NaB acts via GPR43 to reduce the inhibitory Ser495 phosphorylation of CaMKK2 and restore its intrinsic kinase activity, thereby triggering the downstream CaMKK2-AMPKα-SIRT1 signaling cascade. This cascade suppresses the lipogenic transcription factor *SREBP1c* and downstream *FASN* to inhibit de novo lipogenesis, while also upregulating *PGC-1α*, *PPARα*, and *CPT1A* to promote mitochondrial fatty acid oxidation. In parallel with these effects, NaB simultaneously enhances insulin-mediated IRS1-PI3K-AKT signal transduction in hepatocytes. Activated AKT inhibits *FOXO1*, *PCK1*, and *G6PC1* to limit hepatic gluconeogenesis, suppresses *GSK3β* and concurrently activates glycogen synthase (*GS*) to accelerate glycogen synthesis; the putative positive regulatory link between AKT and membrane GLUT2 expression (dotted line in schematic) may boost hepatic glucose uptake. This collective dual-pathway NaB-mediated regulation reduces intrahepatic lipid overload, restores glucose homeostasis, and relieves hepatic insulin resistance in MASLD models. Created by BioRender (Agreement number: TR2A2VB6GT).

Table 1. Serum and hepatic inflammatory factor parameters in HFD-induced MASLD model mice (Mean ± standard deviation, n = 6).

Index	SD	HFD	HFD + LNaB (200 mg/kg)	HFD + HNaB (400 mg/kg)
Serum TNF-α (pg/mL)	62.15 ± 4.38	216.74 ± 12.56*	168.32 ± 9.41$^{\#}$	91.47 ± 6.82$^{\#\triangle}$
Serum IL-6 (pg/mL)	39.27 ± 3.46	206.42 ± 11.85*	138.74 ± 9.16$^{\#}$	59.83 ± 4.75$^{\#\triangle}$
Serum IL-1β (pg/mL)	30.14 ± 2.53	157.36 ± 9.41*	109.28 ± 7.33$^{\#}$	41.52 ± 3.28$^{\#\triangle}$
Serum MCP-1 (pg/mL)	26.35 ± 2.07	141.73 ± 8.69*	97.61 ± 6.94$^{\#}$	33.75 ± 2.61$^{\#\triangle}$
Hepatic TNF-α (pg/mg protein)	54.29 ± 4.05	228.64 ± 13.15*	163.95 ± 9.72$^{\#}$	87.26 ± 5.43$^{\#\triangle}$
Hepatic IL-6 (pg/mg protein)	37.52 ± 3.11	194.37 ± 10.92*	129.46 ± 8.47$^{\#}$	54.68 ± 4.17$^{\#\triangle}$
Hepatic F4/80 mRNA relative expression	1.00 ± 0.08	3.72 ± 0.31*	2.64 ± 0.22$^{\#}$	1.41 ± 0.13$^{\#\triangle}$

Note: All data are presented as mean ± standard deviation, n = 6 mice per group. $^{*}p < 0.05$ vs. SD group; $\#p < 0.05$ vs. HFD group; $\triangle p < 0.05$ vs. HFD + LNaB group. F4/80 expression was normalized to GAPDH. Abbreviations: SD, standard diet; HFD, high-fat diet; LNaB, low-dose sodium butyrate (200 mg/kg); HNaB, high-dose sodium butyrate (400 mg/kg).

incides with parallel improvements in glycolipid metabolic disturbances in MASLD models.

One strength of the present work is the consistency observed between the *in vitro* and *in vivo* findings. In PA-treated HepG2 cells, NaB reduced lipid droplet accumulation and lowered TG, TC, and NEFA levels. In HFD-fed mice, similar changes were observed at the systemic and tissue levels, including lower hepatic TG and TC content, reduced histological evidence of steatosis, and improvements in serum lipid profiles. NaB altered several lipid-related measures rather than solely affecting a single biochemical metric, demonstrating an overall shift toward improved hepatic lipid balance. In MASLD, steatosis is usually the result of combined disturbances in fatty acid entry, lipid synthesis, fatty acid oxidation, and lipid export [21,22].

The IR models used in this study exhibited diminished GPR43 expression, suppressed AMPKα phosphorylation, reduced SIRT1 abundance, and abnormally elevated p-CaMKK2^{Ser495} levels that disrupt CaMKK2-linked signaling. NaB treatment normalized excessive p-CaMKK2^{Ser495} abundance and restored downstream AMPKα phosphorylation. PA lipotoxicity induces excessive phosphorylation of CaMKK2 Ser495 site, which inhibits the activity of CaMKK2 kinase and weakens its phosphorylation activation of AMPKα; NaB intervention can downregulate the inhibitory p-CaMKK2^{Ser495}, restore the basic kinase function of CaMKK2, and ultimately increase the activation level of AMPKα^{Thr172}. In addition, NaB lowered the expression of lipogenic genes including those encoding *SREBP1c* and *FASN*, while increasing the expression of genes involved in fatty acid oxidation and mitochondrial function, including those encoding *PGC-1α*, *PPARα*, and *CPT1A* [16,23]. These molecular changes are consistent with a shift away from lipid synthesis and toward lipid utilization. They also fit with the established role of AMPK as a central energy sensor that restrains lipogenesis and supports fatty acid oxidation in the liver [24,25]. Furthermore, the enrichment of metabolism-related pathways in the NaB-treated group suggests that NaB may help reprogram lipid metabolism to reduce steatosis.

The glucose-related findings in this study were similarly consistent. In the cell model system, PA exposure reduced 2-NBDG uptake, increased intracellular free glucose, and reduced glycogen deposition. Following treatment with NaB, an increase in glucose uptake was noted, together with a decrease in the intracellular free glucose pool and the restoration of glycogen storage. Taken together, these findings suggest a shift from impaired glucose uptake and ineffective intracellular handling toward increased uptake and glycogen storage. The effects of NaB treatment were thus associated with both improved glucose entry into the cell, as well as the more effective downstream utilization of that glucose. A similar pattern was observed in mouse model experiments. NaB treatment improved whole-body glucose homeostasis in HFD-fed mice, with reductions in fasting glucose, 2-h postprandial glucose, fasting insulin, and HOMA-IR, along with better OGTT/IPITT performance, increased QUICKI, and greater hepatic glycogen deposition. The glucose-related effects of NaB noted in HepG2 cells were thus effectively recapitulated in this HFD-induced mouse model.

In peripheral insulin-resistant tissues, impaired GLUT4 membrane translocation is the primary driver of systemic hyperglycemia. However, hepatocytes constitutively express GLUT2 rather than GLUT4. We found that PA-induced lipotoxicity significantly reduced hepatic GLUT2 protein levels, while NaB restored GLUT2 expression and enhanced IRS1/PI3K/AKT phosphorylation. This tissue-specific insulin-dependent regulation of GLUT2 in hepatocytes might be a unique liver metabolic phenotype that distinguishes hepatic insulin resistance from peripheral insulin resistance.

In addition to the observed regulation of hepatic glycolipid homeostasis, our analyses further confirmed the prominent anti-inflammatory effect of NaB both in hepatocytes suffering from lipotoxicity and in HFD-induced MASLD model mice. MASLD is recognized as a typical immunometabolic disease. In this pathological context, excessive intracellular lipid overload activates NF-κB signaling, triggering extensive TNF-α, IL-6, IL-1β, and MCP-1 release, which further exacerbates lipotoxicity and IR via a reciprocal positive feedback loop. *In vivo* animal results provided systemic evidence in support of these effects. Specifically, HFD feeding induced overt increases in levels of peripheral and intrahepatic pro-inflammatory mediators, alongside the upregulation of hepatic F4/80 mRNA indicative of the presence of resident and recruited macrophages. Oral NaB administration downregulated all of the analyzed inflammatory cytokines and reduced F4/80 expression in a dose-dependent manner. This highlights the ability of NaB to alleviate hepatic inflammatory infiltration by restraining macrophage recruitment into the liver parenchyma. These dual regulatory effects of NaB on metabolic and inflammatory activity are interconnected. The alleviation of ectopic lipid deposition eliminates lipid-induced inflammatory stimulation; conversely, the suppression of inflammatory signaling relieves inflammation-mediated impairment of IRS1/PI3K/AKT and AMPK activity, jointly ameliorating hepatic steatosis and IR. The GPR43 receptor may serve as a critical upstream mediator of the anti-inflammatory effects of NaB observed in this study, although targeted inhibition experiments will be necessary to validate this causal association.

NaB treatment resulted in the enhancement of PI3K/AKT signaling, as evidenced by the increased phosphorylation of IRS1, PI3K, and AKT together with elevated GLUT2 expression. The restoration of insulin signaling cascade activity was accompanied by lower *FOXO1*, *PCK1*, and *G6PC1* expression, consistent with reports that PI3K/AKT activation reduces hepatic glucose production

[26,27,28]. Previous studies have evaluated the effects of NaB mainly in relation to either AMPK or PI3K/AKT signaling [29]. In our experiments, both of these pathways were altered under the established cellular and animal IR models and in response to NaB, suggesting that it may exert its effects through the parallel regulation of AMPK and PI3K/AKT signaling rather than either of these pathways in isolation.

Although NaB did not clearly remediate insulin receptor phosphorylation in insulin-resistant HepG2 cells, it nonetheless enhanced downstream IRS1/PI3K/AKT activation and increased GLUT2 expression. In parallel with these effects, NaB reduced the expression of *FOXO1*, *PCK1*, *G6PC1*, and *GSK3β*, while increasing glycogen synthase expression. This pattern is consistent with reduced gluconeogenic drive and enhanced glycogen synthesis, and provides a plausible explanation for why intracellular free glucose levels declined while glycogen content increased following NaB treatment. However, caution is warranted when interpreting these findings as they suggest involvement of the PI3K/AKT pathway, but do not establish direct pathway dependence.

Interplay between the AMPK and PI3K/AKT signaling axes has been described in recent reports [30]. By reducing ectopic lipid accumulation and alleviating lipotoxic stress, AMPK activation can enhance insulin sensitivity, thereby increasing IRS1 phosphorylation and downstream AKT activity. Conversely, AKT activation may indirectly promote mitochondrial biogenesis and fatty acid oxidation via mTORC2–PGC-1α signaling. Our findings suggest that NaB can simultaneously activate the GPR43–CaMKK2–AMPKα-SIRT1 axis and modulate insulin receptor substrate signaling, which may lead to more pronounced metabolic improvements than those associated with influencing either of these pathways individually. Recent multi-omics analyses support this hypothesis, indicating that the simultaneous activation of the AMPK and PI3K/AKT pathways synergistically improves MASLD phenotypes [31,32]. However, this model should be interpreted as a plausible framework rather than a firmly established mechanistic sequence, as no inhibitor or gene-silencing experiments were included in the present study.

These regulatory effects help distinguish the present work from many earlier reports. Previous studies have often focused on a single aspect of the response, emphasizing either AMPK-related lipid regulation or insulin signaling-related glucose control [25,29]. By contrast, our study examined lipid deposition, glucose uptake, intracellular glucose disposition, glycogen storage, and pathway-related signaling within the same MASLD-related insulin resistance setting. Our data suggest that the observed metabolic improvements occurred in parallel with coordinated changes in both of these signaling pathways, improving the overall internal coherence of these results.

NaB is an essential SCFA produced by the microbial fermentation of dietary fiber in the gut [33]. It functions as an energy substrate for colonocytes and modulates host metabolism via GPR43/41 and HDAC inhibition [34,35]. Recent studies have revealed that elevated SCFA levels restore intestinal barrier integrity, reduce endotoxemia, and improve metabolic inflammation in MASLD [36]. Although the present study did not directly measure gut microbiota composition or circulating SCFA levels, the observed GPR43–AMPK activation is consistent with microbiota-mediated NaB effects previously reported *in vivo*. Future studies incorporating microbiome-focused analyses will be crucial to clarify the contributions of the gut–liver axis to the therapeutic effects of NaB.

It is also important to interpret the effects of NaB in the context of other metabolic interventions that have been reported to influence these same pathways. Agents such as metformin and glucagon-like peptide-1 receptor agonists have been linked to AMPK-related and PI3K/AKT-related improvements in fatty liver or insulin-resistant states [37,38]. However, lipid metabolism and glucose handling are often discussed separately for these interventions [39,40]. We do not assert the superiority of NaB relative to these other interventions, but rather seek to provide a more integrated view of how NaB may be associated with metabolic improvement at the phenotypic, biochemical, transcriptional, and signaling levels.

The GPR43/CaMKK2/AMPKα/SIRT1 cascade proposed in our graphical abstract remains a hypothetical upstream signaling axis. We only detected the upregulation of GPR43, CaMKK2, and p-AMPKα protein levels after NaB treatment. No functional experiments such as GPR43 silencing or the use of specific GPR43 antagonists were conducted to clarify whether this receptor is necessary to mediate the hepatic metabolic benefits of NaB administration.

Taken together, our results show that NaB attenuates hepatic steatosis and IR in experimental MASLD models. The observed improvements appear to involve AMPK and PI3K/AKT metabolic signaling, contributing to downstream changes in lipid synthesis, fatty acid oxidation, gluconeogenesis, and glycogen storage. These findings support a potential role for NaB in correcting disordered hepatic glycolipid metabolism, although the underlying regulatory mechanisms and clinical value will require further investigation.

5. Limitations

This study has several limitations that should be considered when interpreting our results:

1. The *in vitro* IR model was constructed using transformed HepG2 hepatoblastoma cells rather than primary murine or human hepatocytes. HepG2 cells carry features of tumor-specific metabolic reprogramming, leading to abnormal glucose and lipid handling compared with normal

primary hepatocytes, which limits the physiological extrapolation of our *in vitro* experimental results.

2. While we observed concurrent changes in AMPK and PI3K/AKT signaling after NaB treatment, we did not conduct any corresponding loss-of-function interventions using pathway inhibitors, gene silencing, or knockout models. Thus, we cannot confirm causal or coordinated regulatory crosstalk between the two pathways.

3. The proposed upstream GPR43/CaMKK2 axis remains hypothetical. No GPR43 blockade or knockdown experiments were performed to verify the indispensable role of this pathway as a mediator of the hepatic effects of NaB administration.

4. Animal experiments used a total of 6 mice per group; formal statistical power calculations were not conducted before animals were randomly assigned to groups, potentially reducing statistical sensitivity to detect mild metabolic differences between intervention groups.

5. Gut microbiota and circulating SCFA concentrations were not measured, meaning that there remains a lack of direct evidence for gut-liver axis crosstalk triggered by NaB *in vivo*.

6. Only male C57BL/6 mice were used for animal experiments, precluding any examination of sex-dependent metabolic differences under conditions of HFD stimulation.

7. No clinical human liver samples were included to validate the translational value of our preclinical findings. This should be taken into consideration when generalizing the metabolic regulatory mechanism of NaB in MASLD to the patient setting.

8. Although key pro-inflammatory cytokines (TNF-α, IL-6, IL-1β, MCP-1) and the macrophage marker F4/80 were quantified in our experimental models, we did not perform immunohistochemical staining for F4/80/CD68 to visualize intrahepatic macrophage infiltration, nor did we detect downstream NF-κB inflammatory signaling-related protein expression, limiting any deeper mechanistic interpretation of the anti-inflammatory pathways associated with NaB administration.

6. Conclusion

Overall, these results suggest that NaB is associated with reduced lipid accumulation, improved glucose uptake and glycogen storage, and the alleviation of IR in experimental MASLD. These changes were accompanied by molecular changes consistent with improved AMPK-related lipid metabolic regulation and PI3K/AKT-related insulin signaling. Overall, the findings suggest that NaB may act as a metabolic modulator in MASLD by coordinately improving hepatic lipid and glucose metabolism, providing an experimental basis for further mechanistic and translational studies. NaB also exerted dose-dependent anti-inflammatory effects, as evidenced by reductions in hepatic and circulating pro-inflammatory cytokine levels and macrophage marker expression, highlighting its comprehensive regulatory role in both metabolic and inflammatory lesions associated with MASLD. Further translational research is warranted to validate these multi-target protective effects in human liver samples. It is also important to note that, without pharmacological inhibition or gene knockout assays targeting the AMPK and PI3K/AKT cascades, we cannot confirm the coordinated regulation of these two signaling pathways by NaB, such that the present results are only observational analyses of relevant changes in pathway activity.

Abbreviations

AUC, area under the curve; AKT, protein kinase B; AMPK, adenosine monophosphate-activated protein kinase; BCA, bicinchoninic acid; CaMKK2, calcium/calmodulin-dependent protein kinase kinase 2; CCK-8, Cell Counting Kit-8; CPT1A, carnitine palmitoyltransferase 1A; DMEM, Dulbecco's Modified Eagle Medium; FBG, fasting blood glucose; FASN, fatty acid synthase; FOXO1, forkhead box O1; G6PC1, glucose-6-phosphatase catalytic subunit 1; GLUT2, glucose transporter 2; GPR43, G protein-coupled receptor 43; GS, glycogen synthase; GSK3β, glycogen synthase kinase 3β; HbA1c, glycated hemoglobin; HDAC, histone deacetylase; HDL-C, high-density lipoprotein cholesterol; HFD, high-fat diet; HOMA-IR, homeostasis model assessment of insulin resistance; INSR, insulin receptor; IPITT, intraperitoneal insulin tolerance test; IR, insulin resistance; IRS, insulin receptor substrate; KEGG, Kyoto Encyclopedia of Genes and Genomes; LDL-C, low-density lipoprotein cholesterol; LKB1, liver kinase B1; MASLD, metabolic dysfunction-associated steatotic liver disease; NaB, sodium butyrate; NAFLD, non-alcoholic fatty liver disease; NEFA, non-esterified fatty acid; OGTT, oral glucose tolerance test; PA, palmitate; PAS, periodic acid-Schiff; PBG, postprandial blood glucose; PCK1, phosphoenolpyruvate carboxykinase 1; PGC-1α, peroxisome proliferator-activated receptor gamma coactivator 1-alpha; PI3K, phosphoinositide 3-kinase; PPARα, peroxisome proliferator-activated receptor α; RT-qPCR, Reverse transcription-quantitative polymerase chain reaction; QUICKI, quantitative insulin sensitivity check index; RNA-seq, RNA sequencing; SCFA, short-chain fatty acid; SD, standard diet; SIRT1, sirtuin 1; SREBP-1c, sterol regulatory element-binding protein 1c; TC, total cholesterol; TG, triglyceride; TNF-α, Tumor Necrosis Factor-α; IL-6, Interleukin-6; IL-1β, Interleukin-1β; MCP-1, Monocyte Chemoattractant Protein-1.

Availability of Data and Materials

The original contributions presented in the study are included in the article/supplementary material. Further inquiries can be directed to the corresponding author. The datasets generated and analysed during the current study are available in the [GEO] repository, [GSE325422].

Author Contributions

YNZ: Writing – review & editing, Writing – original draft, Visualization, Validation, Supervision, Software, Resources, Project administration, Methodology, Investigation, Formal analysis, Data curation, Conceptualization. PJ: Supervision, Writing – review & editing, Writing – original draft, Software, Methodology, Formal analysis. YWZ: Writing – review & editing, Writing – original draft, Methodology, Data curation. YW: Writing – review & editing, Writing – original draft, Methodology, Data curation. YGW: Writing – review & editing, Writing – original draft, Methodology, Formal analysis. GYY: Writing – review & editing, Writing – original draft, Methodology, Formal analysis, Data curation, Conceptualization. All authors contributed to editorial changes in the manuscript. All authors read and approved the final manuscript. All authors have participated sufficiently in the work and agreed to be accountable for all aspects of the work.

Ethics Approval and Consent to Participate

All animal procedures were conducted in accordance with the Laboratory animal—Guideline for ethical review of animal welfare (GB/T 35892-2018) of the People's Republic of China and relevant institutional guidelines for the care and use of laboratory animals. The animal study protocol was approved by the animal ethics committee at the Clinical Medical College of Qinghai University (P-SL-2025-024) on August 12, 2025. The study was carried out in accordance with the ARRIVE guidelines.

Acknowledgment

We gratefully acknowledge the technical assistance provided during the experimental work and thank the Basic Medical Research Center of Qinghai University for providing the experimental platform and support that facilitated this research.

Funding

This research received no external funding.

Conflicts of Interest

The authors declare no conflicts of interest.

Supplementary Material

Supplementary material associated with this article can be found, in the online version, at https://doi.org/10.31083/FBL55577.

References

[1] Younossi ZM, Golabi P, Paik JM, Henry A, Van Dongen C, Henry L. The global epidemiology of nonalcoholic fatty liver disease (NAFLD) and nonalcoholic steatohepatitis (NASH): a systematic review. Hepatology (Baltimore, Md.). 2023; 77: 1335–1347. https://doi.org/10.1097/HEP.0000000000000004

[2] Bo T, Gao L, Yao Z, Shao S, Wang X, Proud CG, et al. Hepatic selective insulin resistance at the intersection of insulin signaling and metabolic dysfunction-associated steatotic liver disease. Cell Metabolism. 2024; 36: 947–968. https://doi.org/10.1016/j.cmet.2024.04.006

[3] Romanos M, Garcia Cordova JM, Villamarin J, Pazmino Zurita JD, Acosta A. Obesity and Metabolic Dysfunction-Associated Steatotic Liver Disease (MASLD): A Literature Review on Pathophysiology and Treatment. Diabetes, Obesity & Metabolism. 2026; 28 Suppl 2: 19–30. https://doi.org/10.1111/dom.70659

[4] Holleboom AG, Francque SM, Cusi K, Caussy C. Close multilevel links between metabolic dysfunction-associated steatotic liver disease and type 2 diabetes mellitus. Metabolism Open. 2025; 28: 100424. https://doi.org/10.1016/j.metop.2025.100424

[5] Goto H, Takamura T. Metabolic Dysfunction-Associated Steatotic Liver Disease Complicated by Diabetes: Pathophysiology and Emerging Therapies. Journal of Obesity & Metabolic Syndrome. 2025; 34: 224–238. https://doi.org/10.7570/jomes25017

[6] Sualeheen A, Tan SY, Georgousopoulou E, Daly RM, Tierney AC, Roberts SK, et al. Mediterranean diet for the management of metabolic dysfunction-associated steatotic liver disease in non-Mediterranean, Western countries: What's known and what's needed? Nutrition Bulletin. 2024; 49: 444–462. https://doi.org/10.1111/nbu.12707

[7] Tao SH, Lei YQ, Tan YM, Yang YB, Xie WN. Chinese herbal formula in the treatment of metabolic dysfunction-associated steatotic liver disease: current evidence and practice. Frontiers in Medicine. 2024; 11: 1476419. https://doi.org/10.3389/fmed.2024.1476419

[8] Jiang S, Zhai L, Shao Y, Sun F, Liu X. Targeting the PI3K/AKT signaling pathway: an important molecular mechanism of herbal medicine in the treatment of MASLD/MASH. Frontiers in Nutrition. 2026; 12: 1743899. https://doi.org/10.3389/fnut.2025.1743899

[9] Feng J, MengHuan L, TingTing Y, XueJie Y, HaiNing G. Research progress on AMPK in the pathogenesis and treatment of MASLD. Frontiers in Immunology. 2025; 16: 1558041. https://doi.org/10.3389/fimmu.2025.1558041

[10] Ortiz-Huidobro RI, Larqué C, Velasco M, Chávez-Maldonado JP, Sabido J, Sanchez-Zamora YI, et al. Sexual dimorphism in the molecular mechanisms of insulin resistance during a critical developmental window in Wistar rats. Cell Communication and Signaling : CCS. 2022; 20: 154. https://doi.org/10.1186/s12964-022-00965-6

[11] Wang K, Shen H, Shi J, Fu J. Harnessing Natural Products as AMPK Activators: A Promising Therapeutic Avenue for Metabolic Dysfunction-Associated Steatotic Liver Disease. Revista Brasileira de Farmacognosia. 2026; 36: 78. https://doi.org/10.1007/s43450-026-00766-9

[12] Kalpana K, Sathiya Priya C, Dipti N, Vidhya R, Anuradha CV. Supplementation of scopoletin improves insulin sensitivity by attenuating the derangements of insulin signaling through AMPK. Molecular and Cellular Biochemistry. 2019; 453: 65–78. https://doi.org/10.1007/s11010-018-3432-7

[13] Su Y, Luo S, Li W, Cheng C, Liu W, Yang X, et al. Chinese Herbal Medicines for Diabetic Cardio-Cerebrovascular Diseases: Key Bioactive Metabolites and Action Mechanisms. Journal of Nutrition and Metabolism. 2026; 2026: 5563248. https://doi.org/10.1155/jnme/5563248

[14] Huang LJ, Wang MY, Xin FZ, Yang RX, Zeng J, Ren TY, et al. Sodium butyrate ameliorates liver fibrosis in metabolic dysfunction-associated steatohepatitis rats via miR-155-5p/SOCS1/PDGF signaling pathway. Hepatobiliary & Pan-

creatic Diseases International : HBPD INT. 2025; 24: 423–432. https://doi.org/10.1016/j.hbpd.2025.04.006

[15] Amiri P, Arefhosseini S, Bakhshimoghaddam F, Jamshidi Gurvan H, Hosseini SA. Mechanistic insights into the pleiotropic effects of butyrate as a potential therapeutic agent on NAFLD management: A systematic review. Frontiers in Nutrition. 2022; 9: 1037696. https://doi.org/10.3389/fnut.2022.1037696

[16] Zheng M, Yang X, Wu Q, Gong Y, Pang N, Ge X, et al. Butyrate Attenuates Hepatic Steatosis Induced by a High-Fat and Fiber-Deficient Diet via the Hepatic GPR41/43-CaMKII/HDAC1-CREB Pathway. Molecular Nutrition & Food Research. 2023; 67: e2200597. https://doi.org/10.1002/mnfr.202200597

[17] Rios-Morales M, Vieira-Lara MA, Homan E, Langelaar-Makkinje M, Gerding A, Li Z, et al. Butyrate oxidation attenuates the butyrate-induced improvement of insulin sensitivity in myotubes. Biochimica et Biophysica Acta. Molecular Basis of Disease. 2022; 1868: 166476. https://doi.org/10.1016/j.bbadis.2022.166476

[18] Zhao T, Gu J, Zhang H, Wang Z, Zhang W, Zhao Y, et al. Sodium Butyrate-Modulated Mitochondrial Function in High-Insulin Induced HepG2 Cell Dysfunction. Oxidative Medicine and Cellular Longevity. 2020; 2020: 1904609. https://doi.org/10.1155/2020/1904609

[19] He Z, Xiong H, Cai Y, Chen W, Shi M, Liu L, et al. Clostridium butyricum ameliorates post-gastrectomy insulin resistance by regulating the mTORC1 signaling pathway through the gut-liver axis. Microbiological Research. 2025; 297: 128154. https://doi.org/10.1016/j.micres.2025.128154

[20] Shapira E, Voinsky I, Klin H, Gurwitz D. Butyrate-Mediated Upregulation of Insulin Pathway Gene Expression Suggests Potential Antidiabetic Effects. Drug Development Research. 2025; 86: e70203. https://doi.org/10.1002/ddr.70203

[21] Kwon S, Jeyaratnam R, Kim KH. Targeting ketone body metabolism to treat fatty liver disease. Journal of Pharmacy & Pharmaceutical Sciences : a Publication of the Canadian Society for Pharmaceutical Sciences, Societe Canadienne des Sciences Pharmaceutiques. 2024; 27: 13375. https://doi.org/10.3389/jpps.2024.13375

[22] Steinberg GR, Carpentier AC, Wang D. MASH: the nexus of metabolism, inflammation, and fibrosis. The Journal of Clinical Investigation. 2025; 135: e186420. https://doi.org/10.1172/JCI186420

[23] Cook KJ, Coulter A, Keenan M, Greenway F, Losso JN. Sodium Propionate or Sodium Butyrate Promotes Fatty Acid Oxidation in HepG2 Cells Under Oxidative Stress. Journal of Medicinal Food. 2023; 26: 74–79. https://doi.org/10.1089/jmf.2021.0120

[24] Fang C, Pan J, Qu N, Lei Y, Han J, Zhang J, et al. The AMPK pathway in fatty liver disease. Frontiers in Physiology. 2022; 13: 970292. https://doi.org/10.3389/fphys.2022.970292

[25] Zhang J, Liu Z, Yin X, Wang E, Wang J. NSC48160 targets AMPKα to ameliorate nonalcoholic steatohepatitis by inhibiting lipogenesis and mitochondrial oxidative stress. iscience. 2023; 27: 108614. https://doi.org/10.1016/j.isci.2023.108614

[26] Saltiel AR, Kahn CR. Insulin signalling and the regulation of glucose and lipid metabolism. Nature. 2001; 414: 799–806. https://doi.org/10.1038/414799a

[27] Roy JR, Janaki CS, Jayaraman S, Veeraraghavan VP, Periyasamy V, Balaji T, et al. Hypoglycemic Potential of *Carica papaya* in Liver Is Mediated through IRS-2/PI3K/SREBP-1c/GLUT2 Signaling in High-Fat-Diet-Induced Type-2 Diabetic Male Rats. Toxics. 2023; 11: 240. https://doi.org/10.3390/toxics11030240

[28] Liu J, Jing C, Guo Y, Shang Z, Zhang B, Zhou X, et al. The central signaling pathways related to metabolism-regulating hormones of the gut-brain axis: a review. Journal of Translational Medicine. 2025; 23: 648. https://doi.org/10.1186/s12967-025-06656-3

[29] Ding J, Liu J, Chen J, Cheng X, Cao H, Guo X, et al. Sodium butyrate alleviates free fatty acid-induced steatosis in primary chicken hepatocytes via the AMPK/PPARα pathway. Poultry Science. 2024; 103: 103482. https://doi.org/10.1016/j.psj.2024.103482

[30] Yuan F, Gao Q, Tang H, Shi J, Zhou Y. Ophiopogonin-B targets PTP1B to inhibit the malignant progression of hepatocellular carcinoma by regulating the PI3K/AKT and AMPK signaling pathways. Molecular Medicine Reports. 2022; 25: 122. https://doi.org/10.3892/mmr.2022.12638

[31] Geng Y, Liu L, Sun Y, Guo L, Wu Y, Jia Z. Metabolic dysregulation in MASLD-associated HCC: diagnostic biomarkers and therapeutic opportunities. Frontiers in Medicine. 2025; 12: 1705723. https://doi.org/10.3389/fmed.2025.1705723

[32] Yuan H, Jung ES, Chae SW, Jung SJ, Daily JW, Park S. Biomarkers for Health Functional Foods in Metabolic Dysfunction-Associated Steatotic Liver Disorder (MASLD) Prevention: An Integrative Analysis of Network Pharmacology, Gut Microbiota, and Multi-Omics. Nutrients. 2024; 16: 3061. https://doi.org/10.3390/nu16183061

[33] Koh A, De Vadder F, Kovatcheva-Datchary P, Bäckhed F. From Dietary Fiber to Host Physiology: Short-Chain Fatty Acids as Key Bacterial Metabolites. Cell. 2016; 165: 1332–1345. https://doi.org/10.1016/j.cell.2016.05.041

[34] Kasubuchi M, Hasegawa S, Hiramatsu T, Ichimura A, Kimura I. Dietary gut microbial metabolites, short-chain fatty acids, and host metabolic regulation. Nutrients. 2015; 7: 2839–2849. https://doi.org/10.3390/nu7042839

[35] Fellows R, Denizot J, Stellato C, Cuomo A, Jain P, Stoyanova E, et al. Microbiota derived short chain fatty acids promote histone crotonylation in the colon through histone deacetylases. Nature Communications. 2018; 9: 105. https://doi.org/10.1038/s41467-017-02651-5

[36] Hao P, Yang X, Yin W, Wang X, Ling Y, Zhu M, et al. A study on the treatment effects of *Crataegus pinnatifida* polysaccharide on non-alcoholic fatty liver in mice by modulating gut microbiota. Frontiers in Veterinary Science. 2024; 11: 1383801. https://doi.org/10.3389/fvets.2024.1383801

[37] En Q, Zeping H, Yuetang W, Xu W, Wei W. Metformin alleviates the calcification of aortic valve interstitial cells through activating the PI3K/AKT pathway in an AMPK dependent way. Molecular Medicine (Cambridge, Mass.). 2021; 27: 156. https://doi.org/10.1186/s10020-021-00416-x

[38] Li W, Zhang X, Song J, Yang L, Wang D, Yuan G, et al. Mechanistic insights into GLP-1 receptor agonist-induced weight loss through ceRNA network analysis. Genomics. 2025; 117: 110988. https://doi.org/10.1016/j.ygeno.2025.110988

[39] Zhang SJ, Xu K, Zhu F, Chen JG, Zhang Y, Teng YQ, et al. Glucagon-Like Peptide-2 Ameliorates Lipid Metabolism in Metabolic Dysfunction-Associated Steatotic Liver Disease Through the Adiponectin-Adiponectin Receptor-Mediated AMPK/PPARalpha Pathway. Physiological Research. 2026; 75: 113–126. https://doi.org/10.33549/physiolres.935711

[40] Winther-Sørensen M, Rasmussen C, Trammell SAJ, Hansen C, Vyberg M, Serizawa R, et al. Distinct and complementary metabolic effects of GLP-1 and glucagon receptor agonism in diet-induced obese mice. Peptides. 2026; 195: 171462. https://doi.org/10.1016/j.peptides.2025.171462